

This work was written as part of one of the author's official duties as an Employee of the United States Government and is therefore a work of the United States Government. In accordance with 17 U.S.C. 105, no copyright protection is available for such works under U.S. Law. Access to this work was provided by the University of Maryland, Baltimore County (UMBC) ScholarWorks@UMBC digital repository on the Maryland Shared Open Access (MD-SOAR) platform.

Please provide feedback

Please support the ScholarWorks@UMBC repository by emailing scholarworks-group@umbc.edu and telling us what having access to this work means to you and why it's important to you. Thank you.



Variability of Upstream Proton Cyclotron Wave Properties and Occurrence at Mars observed by MAVEN

O. M. Romeo^{1,2}, N. Romanelli^{1,3}, J. R. Espley¹, C. Mazelle⁴, G. A. DiBraccio¹, J. R. Gruesbeck¹, and J. S. Halekas⁵

¹NASA Goddard Space Flight Center, Greenbelt, MD, United States.

²CRESST II, University of Maryland, College Park, MD, United States.

³CRESST II, University of Maryland, Baltimore County, Baltimore, MD, United States.

⁴Institut de Recherche en Astrophysique et Planétologie, CNRS - University of Toulouse - UPS - CNES, Toulouse, France

⁵Department of Physics and Astronomy, University of Iowa, Iowa City, Iowa, United States.

Key Points:

- We confirm an annual periodicity of PCW occurrence rate upstream from the Martian bow shock between October 2014 through February 2020
- We report a decrease in median wave amplitude for each consecutive Martian perihelion based on available sampling of Martian upstream region
- PCWs occur more frequently near perihelion for low to intermediate IMF cone angles, slower solar wind speeds and higher solar wind densities

Corresponding author: Orlando Romeo, oromeo@umd.edu, <https://orcid.org/0000-0002-4559-2199>

This article has been accepted for publication and undergone full peer review but has not been through the copyediting, typesetting, pagination and proofreading process, which may lead to differences between this version and the [Version of Record](#). Please cite this article as [doi: 10.1029/2020JA028616](https://doi.org/10.1029/2020JA028616).

This article is protected by copyright. All rights reserved.

Abstract

The presence of plasma waves upstream from the Martian bow shock, with frequencies near the local proton cyclotron frequency in the spacecraft frame, constitutes, in principle, an indirect signature for the existence of planetary protons from the ionization of Martian exospheric hydrogen. In this study, we determine the ‘proton cyclotron wave’ (PCW) occurrence rate between October 2014 through February 2020, based on Magnetometer (MAG) and Solar Wind Ion Analyzer (SWIA) measurements from the Mars Atmosphere and Volatile Evolution (MAVEN) mission. We characterize its dependence on several wave and solar wind (SW) properties, and solar longitude ranges. We confirm a previously reported long-term trend with more PCWs near perihelion, likely associated with changes in exospheric hydrogen density. Furthermore, we report for the first time a decrease in median PCW amplitude for each consecutive Martian perihelion. Such variability cannot be attributed to differences in the distribution of SW conditions. This trend could be associated with changes in solar inputs, foreshock effects, and asymmetries due to the SW convective electric field influencing newborn protons. In addition, we observe PCWs more frequently for low to intermediate interplanetary magnetic field (IMF) cone angles, slower SW speeds, and higher SW proton densities. The IMF cone angle preference likely results from the trade-off between associated linear wave growth rates, wave saturation energies, and pick-up proton densities. Moreover, the dependencies on SW speed and density indicate the importance of the characteristic SW transit timescale and the charge exchange process coupling SW protons with the hydrogen exosphere.

1 Introduction

The solar wind (SW) interacts directly with the atmosphere and ionosphere of several solar system bodies lacking a global intrinsic magnetic field. Such coupling has been observed for active comets, Venus, and Mars (e.g., Acuña et al., 1998; Mazelle & Neubauer, 1993; Tsurutani, 1991; T. L. Zhang et al., 2008). In the Martian environment, the ionosphere and exosphere act as an obstacle to slow down the incoming supermagnetosonic SW, forming a bow shock with a stand-off distance of about $1.6R_M$ (Martian radii) from the center of the planet (Mazelle et al., 2004). Given that the hydrogen (H) exosphere extends beyond this boundary, neutral particles are ionized in the upstream region of Mars. The resulting newborn planetary protons are picked up by the magnetized SW

51 flow, contributing to the planet's atmospheric loss (Chaffin et al., 2015; Chaufray et al.,
 52 2008; Jakosky et al., 2015; Yamauchi et al., 2015). These ions are the result of charge
 53 exchange, photoionization, or electron impact processes that affect the Martian H ex-
 54 osphere (M. H. G. Zhang et al., 1993).

55 Initially, the newborn protons are approximately at rest with respect to Mars. Thus,
 56 seen from the SW reference frame, these ions have a mean velocity approximately equal
 57 to $-\mathbf{v}_{SW}$, where \mathbf{v}_{SW} is the solar wind velocity. The particles drift along the interplan-
 58 etary magnetic field (IMF) \mathbf{B} with a parallel velocity component $v_{\parallel}^i = -v_{SW}\cos(\alpha)$,
 59 where $v_{SW} = |\mathbf{v}_{SW}|$ and α is the angle between \mathbf{v}_{SW} and \mathbf{B} , defined as the IMF cone
 60 angle. Additionally, the planetary ions gyrate about the IMF, with a perpendicular ve-
 61 locity component $v_{\perp}^i = -v_{SW}\sin(\alpha)$ and gyrofrequency $\Omega_i = q_i|\mathbf{B}|/m_i$, where q_i and
 62 m_i denote the ion charge and mass, respectively. Under these conditions, the resulting
 63 proton velocity distribution, consisting of a SW core and newborn ions, is most often highly
 64 unstable, capable of giving rise to several low frequency electromagnetic plasma wave
 65 modes (Brinca, 1991; Lee, 1989; Wu & Davidson, 1972; Wu & Hartle, 1974). In partic-
 66 ular, the interaction between planetary protons and the SW can excite the electromag-
 67 netic ion-ion right-hand (RH) and left-hand (LH) resonant instability modes depending,
 68 among other factors, on the IMF cone angle α .

69 The LH resonant instability has larger linear wave growth rates for large IMF cone
 70 angles and can be associated with related ring-beam or ring pick-up proton velocity dis-
 71 tribution functions (Brinca & Tsurutani, 1989; Gary & Madland, 1988). In contrast, the
 72 RH resonant instability is in many cases the most easily excited mode for low to mod-
 73 erate IMF cone angles, associated with proton beam or ring-beam distributions (Gary,
 74 1993). For both resonant instabilities, the observed wave frequency is Doppler-shifted
 75 due to the relative motion between the spacecraft (SC) and SW reference frames. As the
 76 spacecraft has a negligible planetocentric velocity compared to \mathbf{v}_{SW} , the observed wave
 77 frequency ω_{SC} in the SC reference frame is

$$\omega_{SC} = \omega - \mathbf{k} \cdot \mathbf{v}_{\parallel}^{SC} \quad (1)$$

78 where ω is the wave frequency, \mathbf{k} is the wave vector, and $\mathbf{v}_{\parallel}^{SC} = -[\mathbf{v}_{SW} \cdot \hat{\mathbf{k}}] \hat{\mathbf{k}}$ is the
 79 spacecraft's velocity parallel to the wave propagation direction. Additionally, the expected

80 wave frequency in the newborn ion reference frame is $\omega_i = \omega - \mathbf{k} \cdot \mathbf{v}^i$ for both the RH
 81 and LH modes, where \mathbf{v}^i is the velocity of the newborn ions in the SW reference frame.

82 In particular, the RH resonant mode satisfies the following cyclotron resonance con-
 83 dition for moderate IMF cone angles:

$$\omega - \mathbf{k} \cdot \mathbf{v}_{\parallel}^i + n\Omega_i = 0, \quad n = 1, 2, 3, \dots \quad (2)$$

84 where \mathbf{v}_{\parallel}^i is the ion drift velocity along the magnetic field (Gary, 1991) in the SW ref-
 85 erence frame. Given that the planetary newborn particles are approximately at rest ini-
 86 tially with respect to Mars, the observed wave frequency in the SC reference frame for
 87 the RH mode is

$$\omega_{SC} = -n\Omega_i \quad (3)$$

88 Thus, the observed frequency ω_{SC} is expected to be near the newborn ion gyrofrequency
 89 for $n = 1$ (fundamental mode), with the opposite polarization from the SW reference
 90 frame. Since the observed frequency is very close to the local proton cyclotron frequency,
 91 these waves are known as ‘proton cyclotron waves’ (PCWs). However, we note that the
 92 term PCW refers to one of the wave’s main observed signatures, and does not correspond,
 93 most of the time, to the ion cyclotron wave mode. The detection of PCWs constitutes,
 94 in principle, an indirect signature of the presence of newborn planetary protons (Brinca,
 95 1991).

96 It is worth noticing that the term corresponding to the Doppler shift in equation
 97 (1) is relatively small for the LH resonant mode. Therefore, waves generated from the
 98 LH instability are also expected to be observed with frequencies very close to the local
 99 ion gyrofrequency and left-hand polarized in the SC frame. In contrast with the RH res-
 100 onant mode, these waves are expected to be left-hand polarized in both the SW and SC
 101 reference frames.

102 PCWs have been observed around Mars by several planetary missions. Russell et
 103 al. (1990) analyzed the first observations of PCWs upstream from the Martian bow shock
 104 with the Phobos 2 spacecraft. Additional studies of upstream PCWs were performed with
 105 data from the Mars Global Surveyor (MGS) and Mars Atmosphere and Volatile Evolu-
 106 tion (MAVEN) missions. These waves have been observed to have frequencies very close

107 to the local proton gyrofrequency, left-handed elliptical polarization in the SC reference
108 frame, propagation angles ($\theta_{kB} \sim 20^\circ$) quasi-parallel to the mean IMF direction, and
109 are approximately planar (e.g., Bertucci et al., 2013; Brain et al., 2002; Liu et al., 2020;
110 Mazelle et al., 2004; Romanelli et al., 2013, 2016; Wei & Russell, 2006; Wei et al., 2011,
111 2014). Among these works, Romanelli et al. (2013) reported the presence of a strong vari-
112 ability in the PCW occurrence rate between two different premapping subphases of the
113 MGS mission. In particular, these changes were not found to be associated with MGS
114 spatial biases or measured IMF cone angle distributions, suggesting that the observed
115 variability in the occurrence rate could be related to temporal changes in properties of
116 the Martian H exosphere.

117 Bertucci et al. (2013) then expanded upon this work, analyzing all premapping or-
118 bits of MGS from September 1997 through September 1998 for altitudes below 20,400
119 km ($6R_M$). PCWs were found more frequently near Martian perihelion and southern sum-
120 mer solstice, with a $\sim 70\%$ increase in average PCW occurrence rate compared to ob-
121 servations during periods close to the southern autumn and spring equinoxes. Bertucci
122 et al. (2013) classified PCW events based on the identification of a clear spectral line in
123 the power spectral density (PSD) of the transverse magnetic field component near the lo-
124 cal proton cyclotron frequency f_c in the SC frame. However, the study did not take into
125 account the polarization properties of the waves nor the PSD of the compressive com-
126 ponent near f_c . These considerations would differentiate quasi-monochromatic wave events
127 from dispersive wave packets generated by steepening of low frequency compressive non-
128 linear waves (Mazelle & Neubauer, 1993). Utilizing MAVEN observations, Romanelli et
129 al. (2016) was able to apply more stringent criteria to identify PCWs, considering both
130 frequency and polarization properties of the waves. Additionally, MAVEN observations
131 upstream from the Martian bow shock allow broader spatial coverage over the planet,
132 given that measurements are not constrained over the Martian south pole as was the case
133 for MGS premapping orbits (Albee et al., 2001). Analyzing MAVEN data between Oc-
134 tober 2014 and March 2016 for about one Martian year, Romanelli et al. (2016) confirmed
135 PCW abundance upstream from the Martian bow shock varies with time, with more waves
136 detected near perihelion. Romanelli et al. (2016) also presented simulated exospheric H
137 density profiles at higher altitudes that display a similar long-term trend, suggesting a
138 coupling with the temporal variability of PCW occurrence rate.

139 Related studies have also reported changes in the Martian neutral and ionized en-
140 vironment on a similar timescale. Chaufray et al. (2015) simulated a 3D temporal model
141 of the H exosphere and thermosphere to investigate the variability in exospheric H den-
142 sity and escape rate due to solar activity and Martian heliocentric distance. Yamauchi
143 et al. (2015) analyzed Ion Mass Analyzer (IMA) data from the Mars Express (MEX) mis-
144 sion, and reported higher pick-up ion detection rates near perihelion for several Martian
145 years, supporting a dependence between PCW occurrence and Martian heliocentric dis-
146 tance. Studies based on MAVEN measurements have shown exospheric H densities (Halekas,
147 2017; Rahmati et al., 2017) and escape rates (Rahmati et al., 2018) increase by an or-
148 der of magnitude for time periods closer to perihelion compared to aphelion. Addition-
149 ally, previous work has shown dust activity and water vapor concentrations high in the
150 lower atmosphere to have an effect on the variability of the H exosphere (Bhattacharyya
151 et al., 2015, 2017; Chaffin et al., 2014, 2017; Clarke et al., 2014, 2017; Fedorova et al.,
152 2018, 2020; Heavens et al., 2018).

153 It is important to note that the MEX instrumental package does not include an
154 onboard magnetometer, which prevents the direct detection of PCWs. In addition, MGS
155 did not possess an onboard SW ion detection instrument to study SW properties dur-
156 ing PCW events. As MAVEN provides both magnetic field and SW measurements, this
157 mission presents an excellent opportunity to perform studies focused on these low fre-
158 quency plasma waves (e.g., Andrés et al., 2020; Halekas et al., 2020; Liu et al., 2020).
159 In this work, we present an extensive study with MAVEN observations covering almost
160 three Martian years, identifying PCW events with strict criteria, to analyze the occur-
161 rence rate variability, main wave properties, and SW conditions that favor their pres-
162 ence. More specifically, we analyze measurements from the magnetometer (MAG) and
163 Solar Wind Ion Analyzer (SWIA) instruments on board the MAVEN spacecraft from
164 October 2014 through February 2020.

165 This study is structured as follows. Section 2 provides information on the MAVEN
166 mission, and the MAVEN MAG and SWIA instruments. A case study of an observed
167 PCW event is also presented in this section. In section 3, we describe the PCW selec-
168 tion criteria based on wave frequency and polarization properties. Section 4 reports the
169 results on temporal variability of PCW abundance, main wave properties, and SW con-
170 ditions favoring PCW generation. With data spanning almost three Martian years, MAVEN
171 observations are grouped separately based on time intervals close to each Martian per-

172 helion and aphelion to analyze wave and SW properties. In addition, the spatial cov-
173 erage of MAVEN is provided in this section. Finally, the discussion and conclusions are
174 presented in sections 5 and 6, respectively.

175 **2 MAVEN Observations of PCW Events Upstream from the Martian** 176 **Bow Shock**

177 **2.1 MAVEN Mission and Instruments**

178 The MAVEN spacecraft was launched in November 2013, arrived at Mars in Septem-
179 ber 2014, and is currently in its extended mission and relay phase. The orbit had a nom-
180 inal periapsis altitude of 150 km, an apoapsis altitude of 6220 km, and a period of about
181 4.5 hours (Jakosky et al., 2015). Currently, the periapsis altitude has been raised and
182 apoapsis lowered to conserve fuel during the relay phase of the mission. The selected apoap-
183 sis altitude, orbital period, and orbital inclination (75°) allow orbital precession in both
184 local time and latitude of the spacecraft periapsis, partially driven by the non-symmetric
185 gravitational field. Additionally, the extent of the MAVEN apoapsis allows sampling of
186 SW properties in many of its orbits.

187 The MAVEN MAG instrument is a dual-fluxgate magnetometer that provides vec-
188 tor magnetic field measurements over a broad range (to 65,536 nT per axis) with a sam-
189 pling frequency of 32 Hz and accuracy of 0.25 nT (Connerney et al., 2015b). Upstream
190 from the Martian bow shock, PCWs are characterized by a relatively low frequency (\sim
191 0.06 Hz for an IMF intensity of ~ 4 nT) in the SC reference frame, compared to the MAG
192 sampling cadence. Thus, in this work, we computed 4 Hz magnetic field averages from
193 the 32 Hz MAG data, sufficient for the purposes of the present study. The MAVEN MAG
194 field components are presented in the Mars-centered Solar Orbital (MSO) coordinate sys-
195 tem, where the X axis is directed toward the Sun, the Z axis is perpendicular to Mars's
196 orbital plane (positive toward the ecliptic north), and the Y axis completes the right-
197 handed system.

198 Observations from SWIA on board MAVEN were also used to characterize SW con-
199 ditions under which the waves are present. SWIA is an energy and angular ion spectrom-
200 eter with electrostatic deflectors that measures ion fluxes over a broad energy range (25
201 eV/q to 25 keV/q) with a wide field of view of $360^\circ \times 90^\circ$ (Halekas et al., 2015). In this
202 analysis, we utilized the onboard-calculated moments of ion distribution functions for

the SW velocity in MSO coordinates and SW density, with a temporal resolution of 4 seconds.

2.2 Case Study: PCW Event on 26 November 2018

Figure 1 presents an example of a proton cyclotron wave event observed by MAVEN MAG and SWIA upstream from the Martian bow shock on 26 November 2018, between 16:12:18 UT and 16:20:50 UT. Figures 1a through 1d display the magnetic field and SW velocity MSO components and magnitude. Clear oscillations with a distinct frequency are observed for all magnetic field components during this time interval with a wave amplitude around 0.3 nT and a mean IMF of $\mathbf{B}_0 = [2.6, -2.4, 0.9]$ nT. For this event, the mean SW velocity is $\mathbf{v}_{SW} = [-344.0, 54.7, 3.6]$ km s⁻¹ and IMF cone angle is $\alpha = 36.0^\circ$, computed from MAG and SWIA measurements. Fluctuations in the SW velocity measurements have a similar frequency to the magnetic field oscillations. Figure 1e shows the ion density derived from SWIA, with a mean density of $n_{SW} = 4.3$ cm⁻³. We find that these waves present a small degree of compressibility with $\sigma_{n_{SW}}/n_{SW} = 0.04$, where $\sigma_{n_{SW}}$ is the standard deviation of the density measurements during this time interval.

Figure 2a shows the PSD of the transverse B_\perp and compressive B_\parallel magnetic field components with respect to \mathbf{B}_0 for the same 512 second time interval in Figure 1. We implement a Hanning window to reduce spectral leakage and ensure a narrow main lobe. The associated local proton cyclotron frequency f_c for $B_0 = 3.7$ nT is 0.056 Hz, denoted by the vertical black line in Figure 2a. The value of $PSD[B_\perp]$ is maximized near f_c at a frequency of 0.051 Hz ($0.91f_c$) and is larger than $PSD[B_\parallel]$ at the same frequency by a factor of ~ 28 .

To determine the polarization and direction of propagation for the detected waves, we apply Minimum Variance Analysis (MVA) for subintervals corresponding to three local proton cyclotron gyroperiods within the 512 second interval (Sonnerup & Scheible, 1998). That is, we require at least three wave periods to identify and characterize waves with MVA. This technique consists of calculating the eigenvalues λ_j and eigenvectors e_j of the covariance matrix for the magnetic field MSO components in each subinterval. The maximum (λ_1), intermediate (λ_2) and minimum (λ_3) eigenvalues can be used to characterize properties of the detected waves. In particular, $\lambda_1/\lambda_2 \sim 1$ and $\lambda_2/\lambda_3 \gg 1$ suggest a detection of circularly polarized and planar waves, respectively. When the assump-

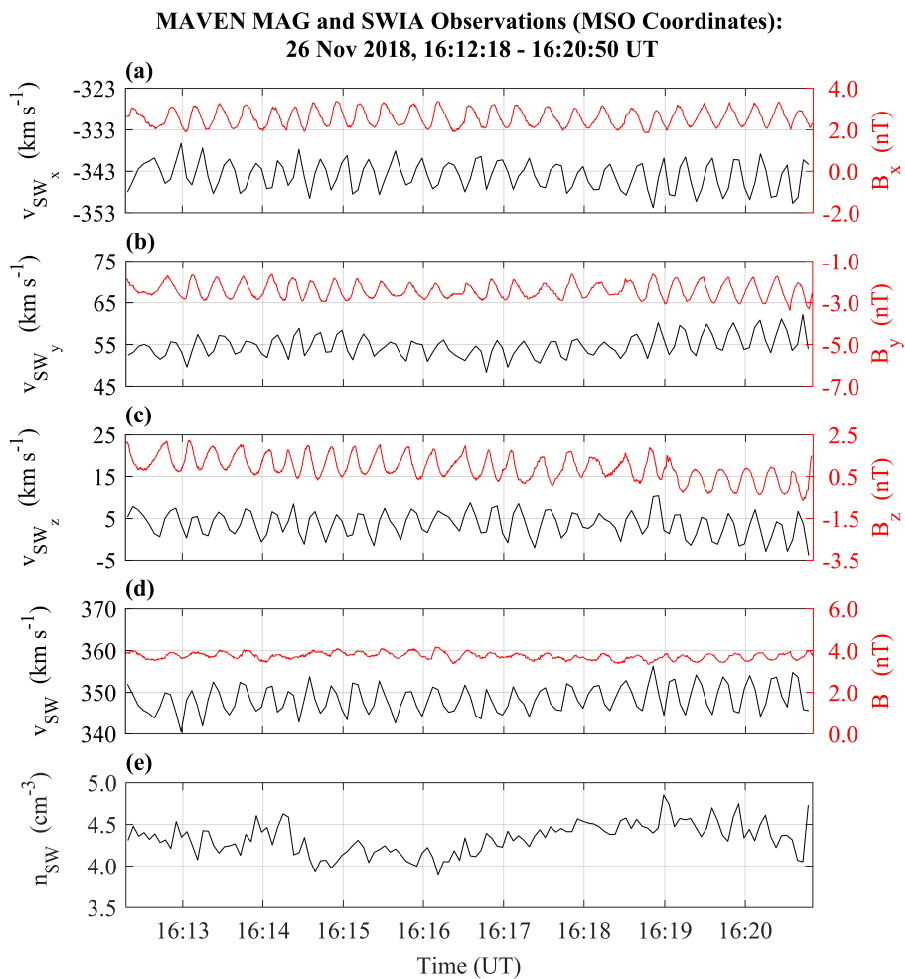


Figure 1. PCW event upstream from the Martian bow shock observed by the MAVEN MAG and SWIA instruments on 26 November 2018, 16:12:18 – 16:20:50 UT. (a–d) The magnetic field (red) and SW velocity (black) components and magnitude in MSO coordinates. (e) The SW ion density.

tion of planar waves is supported by the λ_2/λ_3 ratio, the direction of the wave vector \mathbf{k} can also be approximated by the eigenvector \mathbf{e}_3 associated with the smallest eigenvalue. However, the eigenvector \mathbf{e}_3 only defines the direction of \mathbf{k} and not the sense (Sonnerup & Scheible, 1998). We also apply equations (3.3b, 3.4b, 3.8a) reported in Song and Russell (1999) to determine the wave amplitude δB , described as $\delta B = \sqrt{\lambda_1 - \lambda_3}$.

Figure 2b displays the magnetic field oscillations in the maximum-intermediate plane (hodogram) in the MVA basis ($\mathbf{e}_1, \mathbf{e}_2, \mathbf{e}_3$) for the subinterval 16:14:50 – 16:15:44 UT on 26 November 2018. The mean magnetic field in the MVA basis is $\mathbf{B}_0^{MVA} = [-0.5, -0.7, 3.7]$ nT, directed inwards toward the maximum-intermediate plane. The propagation angle θ_{kB} can be estimated by the angle between \mathbf{e}_3 and \mathbf{B}_0 . We find that θ_{kB} is 16.0° , suggesting that these waves propagate quasi-parallel to the mean magnetic field upstream from the Martian bow shock. This wave event near the local proton cyclotron frequency is approximately circular ($\lambda_1/\lambda_2 = 1.07$) and planar ($\lambda_2/\lambda_3 = 82.52$), with a wave amplitude of $\delta B = 0.5$ nT. Based on the mean rotational direction of the magnetic field oscillations with respect to \mathbf{B}_0^{MVA} (shown by the black arrow in Figure 2b), the wave is found to be left-hand polarized in the SC reference frame. All these results are consistent with previously reported properties of waves very close to the local proton cyclotron frequency upstream from Mars (Connerney et al., 2015a; Bertucci et al., 2013; Brain et al., 2002; Liu et al., 2020; Mazelle et al., 2004; Romanelli et al., 2013, 2016; Ruhunusiri et al., 2015, 2016; Russell et al., 1990; Wei & Russell, 2006; Wei et al., 2011, 2014).

3 PCW Selection Criteria

For this statistical study, we utilize a subset of MAVEN MAG and SWIA data from October 2014 through February 2020 representing 2.8 Martian years of observing time. To identify measurements in the upstream region of Mars, we consider the Martian bow shock fit from Gruesbeck et al. (2018) with an increased semilatus rectum corresponding to a 25% enlarged boundary. This extension of the fit accounts for variable bow shock expansions to ensure upstream wave detection near Mars. The upstream data from both instruments is then divided into 512 second time intervals with 90% overlap between contiguous segments. The length of this interval is sufficient to compute Fast Fourier transforms of PCW events, covering at least ~ 10 wave periods.

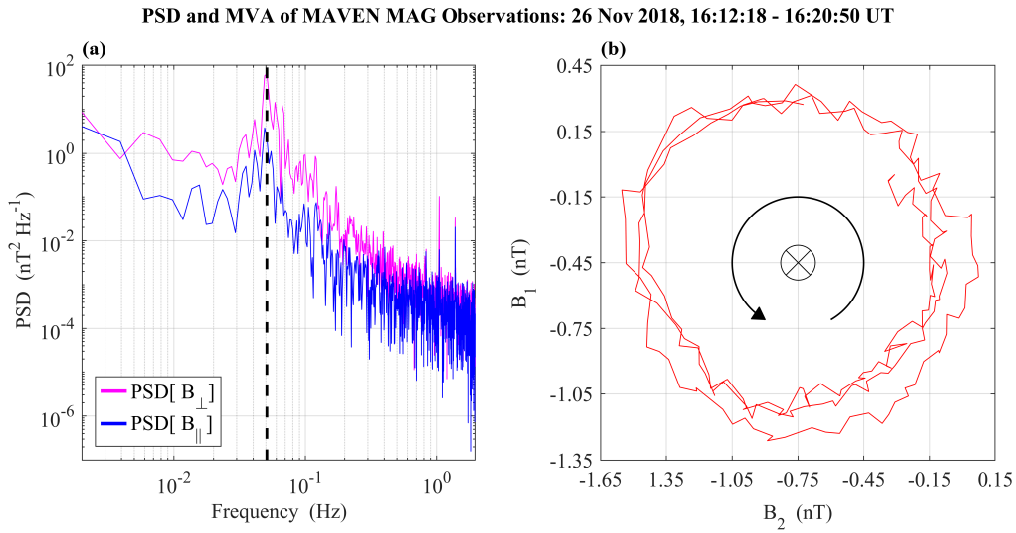


Figure 2. MAVEN MAG observations on 26 November 2018 16:12:18 – 16:20:50 UT for a PCW event. (a) Power spectral density (PSD) of the transverse (blue) and compressive (magenta) magnetic field components, where the dashed vertical line (black) indicates the mean local proton cyclotron frequency f_c . (b) Hodogram of the magnetic field observations in the maximum-intermediate MVA plane for the subinterval 16:14:50 – 16:15:44 UT, covering approximately three local proton cyclotron gyroperiods. The mean magnetic field is directed inwards toward the maximum-intermediate plane and the wave is left-hand polarized in the SC frame.

265 For each upstream 512 second interval, we consider a set of criteria to identify PCW
 266 events based on frequency and polarization properties of the waves. In order to combine
 267 the PSD and MVA techniques for the PCW selection criteria, the wave parameters de-
 268 rived from MVA for each ~ 3 gyroperiod subinterval are averaged over the 512 second
 269 interval. The first necessary condition for a PCW detection is based on the $PSD(f)$ of
 270 B_{\perp} , given by the expressions:

$$PSD[B_{\perp}]_{0.8f_c-\Delta f}^{1.2f_c+\Delta f} > \xi_{\perp} PSD[B_{\perp}]_{1.2f_c+\Delta f}^{1.4f_c+\Delta f} \quad (4a)$$

$$PSD[B_{\perp}]_{0.8f_c-\Delta f}^{1.2f_c+\Delta f} > \xi_{\perp} PSD[B_{\perp}]_{0.6f_c-\Delta f}^{0.8f_c+\Delta f} \quad (4b)$$

271 where the PSD is computed in a frequency interval centered around the local proton cy-
 272 clotron frequency f_c , which must be greater by a factor ξ_{\perp} compared to the PSD for two
 273 neighboring frequency intervals. The uncertainty Δf of f_c is associated with the MAG
 274 instrument's uncertainty ($\Delta B = 0.25$ nT) and is equal to 0.004 Hz. Once the peak in
 275 $PSD[B_{\perp}]$ is located at a frequency f close to the expected frequency f_c , the second cri-
 276 terion is

$$PSD[B_{\perp}]_f > \xi_{\parallel} PSD[B_{\parallel}]_f \quad (5)$$

277 through which we only consider cases with a peak in $PSD[B_{\perp}]$ larger than $PSD[B_{\parallel}]$ by
 278 a factor ξ_{\parallel} .

279 Based on the polarization properties obtained from MVA for each three cyclotron
 280 period subinterval, the third condition to identify PCWs is described by

$$\lambda_2/\lambda_3 > \lambda_{23} \quad (6)$$

281 where the ratio of the eigenvalues for each subinterval is averaged over the 512 second
 282 interval and must be greater than the constant λ_{23} . Finally, we calculate the mean ro-
 283 tation vector of the magnetic field oscillations in the $e_1 - e_2$ plane for each subinter-
 284 val from MVA. Detected waves are expected to have left-handed polarization in the SC
 285 frame, in which the e_3 -component of the mean rotational direction is anti-parallel to the
 286 e_3 -component of the mean magnetic field in the MVA basis. For each three gyroperiod
 287 subinterval s , we compute the scalar product between these two vectors and assign the
 288 resulting sign to the parameter p_s . Left-handed and right-handed polarization in each

subinterval correspond to $p_s = -1$ and $p_s = 1$, respectively. p_s is then averaged over the entire 512 second interval from each subinterval to obtain the average polarization parameter p . Therefore, the fourth criterion to identify a PCW event is satisfied if $p < 0$, indicating that at least 50% of the subintervals are left-hand polarized within the 512 second interval.

To select the values of the constant terms associated with the selection criteria, we evaluated 36 different combinations of $\xi_{\perp} = \{1.0, 1.5, 2.0, 2.5, 3.0, 3.5\}$, $\xi_{\parallel} = \{1, 2, 3\}$ and $\lambda_{23} = \{5, 10\}$. Similar results for PCW temporal variability, main wave properties and favorable SW conditions are observed for $\xi_{\perp} \geq 1.5$, $\xi_{\parallel} \geq 2$, and $\lambda_{23} \geq 5$. Therefore, to ensure reliable results with a sufficient number of total events, we set $\xi_{\perp} = 1.5$, $\xi_{\parallel} = 3$, and $\lambda_{23} = 5$ to identify PCWs in this statistical study.

4 Results

4.1 Temporal Variability of PCW Occurrence Rate Upstream from Mars

From October 2014 through February 2020, we find 529,652 time intervals in the upstream region with available data from both MAG and SWIA instruments. Figure 3a displays a histogram with the number of upstream 512 second intervals as a function of time with bin sizes of 15 terrestrial days. The lack of data in empty bins implies that either MAVEN was not upstream from the Martian bow shock or the instruments were not active. One 15 day bin (November – December 2019) is not considered to determine PCW abundance as it contains a relatively small number of upstream events (78 intervals). All other bins have at least 1,000 intervals, with an average of about 8,000 upstream events per bin. The bins with the lowest (November 2014) and highest (January – February 2019) number of upstream intervals contain 1,160 and 13,184 events, respectively.

Based on the selection criteria discussed in section 3, we identify 50,730 PCW events. We compute the ratio of PCW events to the total number of upstream intervals for each 15 day bin to obtain the PCW occurrence rate as a function of time, shown in Figure 3b. The dashed black line emphasizes time intervals lacking observations upstream from Mars. The occurrence rate of PCWs near each Martian perihelion (PH) and northern winter solstice (NWS) exhibit an increase up to 30% – 35%, significantly larger than the average PCW occurrence rate of $\sim 2\%$ close to aphelion (AH) for each Martian year. Near Martian aphelion, the PCW occurrence rate remains approximately constant below \sim

320 3%. Each of the three main peaks occurs between a Martian solar longitude (L_s) range
 321 of $L_s = 280^\circ - 302^\circ$, slightly after PH ($L_s = 251^\circ$) and NWS ($L_s = 270^\circ$). At the same
 322 time, the main increase in PCW occurrence rate for each year develops during part of
 323 the Martian dust storm season ($L_s = 180^\circ - 360^\circ$), denoted by the gray regions in Fig-
 324 ure 3b. To analyze changes in PCW occurrence, wave properties and SW conditions based
 325 on the Martian heliocentric distance, we group the data into two different sets of time
 326 periods near PH and AH, considering the solar longitude and PCW occurrence rate. MAVEN
 327 data measured within the range $L_s = [215^\circ, 315^\circ]$ are organized into three groups with
 328 high rates (HR) of PCW occurrence for each of the three Martian years (HR1, HR2, HR3)
 329 close to PH. Upstream observations within the range $L_s = [35^\circ, 135^\circ]$ are organized into
 330 three groups with low rates (LR) of PCW occurrence for each of the three Martian years
 331 (LR1, LR2, LR3) close to AH. Additionally, to assess possible seasonal sampling biases,
 332 Figure 3c displays the PCW occurrence rate as a function of the Martian solar longitude
 333 for the three Martian years analyzed. We have defined each Martian year to begin and
 334 end at $L_s = 175^\circ$ based on the L_s ranges for the HR and LR groups, where the orange,
 335 green, and purple points correspond to the first (Y1), second (Y2), and third (Y3) Mar-
 336 tian years.

337 We determined the HR solar longitude range based on PCW occurrence rates greater
 338 than 3%, which is above the maximum rate near each AH. Furthermore, the duration
 339 of the main increase in PCW abundance near PH is slightly different for each of the three
 340 Martian years. Therefore, we set the L_s range for the HR groups to cover all three time
 341 spans with high PCW occurrence rate. The LR solar longitude range is then defined by
 342 subtracting 180° from the HR range. Therefore, the corresponding time periods for the
 343 HR1, HR2, and HR3 groups are 15 October 2014 to 26 March 2015, 1 September 2016
 344 to 10 February 2017, and 20 July 2018 to 29 December 2018, respectively. The time pe-
 345 riods for the LR1, LR2, and LR3 groups are 31 August 2015 to 9 April 2016, 18 July 2017
 346 to 25 February 2018, and 5 June 2019 to 13 January 2020, respectively. PCW occurrence
 347 rates for the HR1, HR2, and HR3 groups are 25% (65,321 upstream intervals), 14% (46,176
 348 upstream intervals), and 16% (99,898 upstream intervals), respectively. Occurrence rates
 349 for the LR1, LR2, and LR3 groups are 2% (47,758 upstream intervals), 1% (40,045 up-
 350 stream intervals), and 2% (31,473 upstream intervals), respectively.

351 As the MAVEN orbit around Mars varies with time, it is important to consider po-
 352 tential effects associated with seasonal sampling when comparing observations at approx-

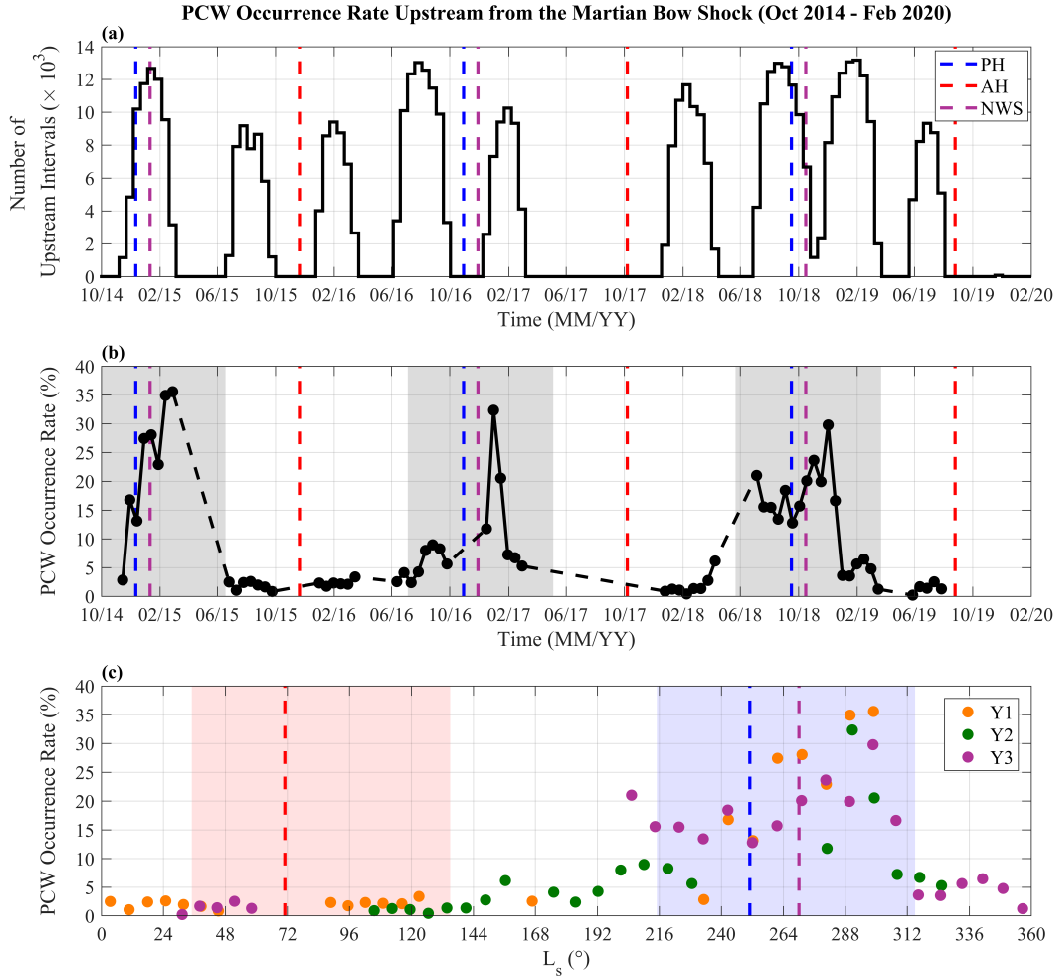


Figure 3. (a) Histogram of the number of 512 second time intervals (in thousands) upstream from the Martian bow shock from October 2014 through February 2020. The blue, purple, and red vertical dashed lines represent Martian perihelion (PH, $L_s = 251^\circ$), northern winter solstice (NWS, $L_s = 270^\circ$), and aphelion (AH, $L_s = 71^\circ$), respectively. (b) PCW occurrence rate (%) as a function of time (black). The dashed black line indicates periods of upstream data gaps observed by MAVEN, and the gray regions correspond to periods of dust storm seasonal activity ($L_s = 180^\circ - 360^\circ$) for each Martian year. (c) PCW occurrence rate (%) as a function of solar longitude, with the orange, green and purple points corresponding to the first (Y1), second (Y2), and third (Y3) Martian years. The red and blue shaded regions represent the solar longitude range for the LR ($L_s = [35^\circ, 135^\circ]$) and HR ($L_s = [215^\circ, 315^\circ]$) groups, respectively.

353 imately the same Martian longitude range. For instance, a larger number of intervals up-
 354 stream from Mars are available for analysis around perihelion and NWS for HR1, com-
 355 pared to HR3. Moreover, the number of upstream intervals increases right after NWS
 356 for HR2. These differences may affect the observed shape and timing of the PCW oc-
 357 currence peak in Figure 3b for each Martian year, when the number of upstream inter-
 358 vals is relatively small. However, as shown in Figure 3c, the three overlapping Martian
 359 years display a clear gradual increase of PCW occurrence rate to a peak slightly after
 360 perihelion and NWS, with steady rates around $\sim 2\%$ close to aphelion.

361 We also conduct an analysis of MAVEN spatial coverage in the upstream region
 362 to determine if the differences in PCW occurrence rate between the HR and LR groups
 363 could be associated with spacecraft sampling biases. We primarily focus on the SC X_{MSO} ,
 364 Z_{MSO} , and altitude positions. Indeed, while the SW velocity is approximately along the
 365 X_{MSO} axis, defining the direction along which PCWs are convected, the Z_{MSO} coor-
 366 dinate sampling might introduce biases due to the asymmetric distribution of Martian
 367 crustal magnetic fields. We also consider spatial changes in the SC altitude over time
 368 as the most likely source of PCWs are ionized, exospheric H atoms whose density de-
 369 cays with the distance to Mars.

370 Figure 4 presents histograms of the normalized number of 512 second time inter-
 371 vals for the HR and LR groups as a function of each MSO spatial coordinate. The or-
 372 bital coverage in the X_{MSO} direction mainly spans within the range $0.5R_M - 2.5R_M$,
 373 with orbits reaching up to $2.8R_M$ for HR3. The distributions shown in Figures 4a and
 374 4e for X_{MSO} are overall similar between the corresponding HR and LR groups. How-
 375 ever, the LR1 histogram is slightly skewed towards lower X_{MSO} values compared to its
 376 HR counterpart. Most of the Y_{MSO} histograms cover a similar range between $-3.0R_M$
 377 and $3.0R_M$, with the exception that the LR1 distribution is mainly sampled for positive
 378 Y_{MSO} . The most variable spatial coverage between the HR and LR groups is associated
 379 with the Z_{MSO} distributions, displayed in Figures 4c and 4g. The histogram for HR1
 380 primarily samples the southern hemisphere, whereas both Martian hemispheres are cov-
 381 ered by MAVEN for LR1. The HR2 histogram also primarily covers the southern hemi-
 382 sphere, while the northern hemisphere is sampled by MAVEN for LR2. Both HR and
 383 LR groups near the third Martian year mainly encompass the northern hemisphere. For
 384 the SC altitude shown in Figures 4d and 4h, most of the HR and LR histograms are very
 385 similar, between $1.0R_M$ and $2.0R_M$, with the exception that the LR3 distribution sam-

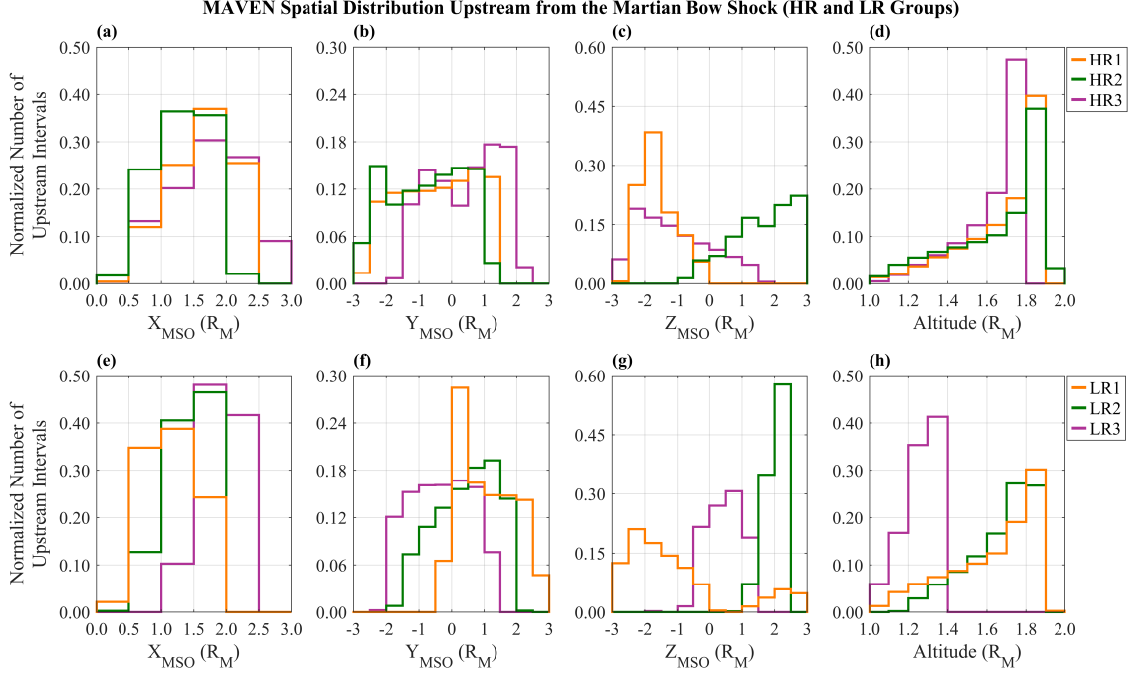


Figure 4. Normalized number of 512 second upstream intervals for HR1 (orange), HR2 (green), and HR3 (purple) as a function of (a) X_{MSO} , (b) Y_{MSO} , (c) Z_{MSO} and (d) altitude. Normalized Number of 512 second time intervals for LR1 (orange), LR2 (green), and LR3 (purple) as a function of (e) X_{MSO} , (f) Y_{MSO} , (g) Z_{MSO} and (h) altitude.

386
387
388
389
 ples primarily lower altitudes. Therefore, Figure 4 suggests that changes in PCW occurrence rate between perihelion and aphelion are not likely attributed to sampling biases in X_{MSO} , Y_{MSO} , and SC altitude as these spatial coordinates show small variability between the three Martian years.

390 4.2 PCW Main Properties

391
392
393
394
395
396
397
398
 In this section, we only consider upstream time intervals identified as PCW events according to the selection criteria given in section 3. We define the PCW probability distribution function $P(x)$ by discretizing the number of PCW events into bins of a given wave property x and normalizing by the total number of PCW intervals. The integral of the function $P(x)$, bounded by the lower and upper limits of x , is equal to one, whereas this is not the case for the observed PCW occurrence rate. Figure 5 displays the PCW probability distribution $P(x)$ upstream from the Martian bow shock from October 2014 through February 2020 for various wave properties derived from MVA. The bin sizes for

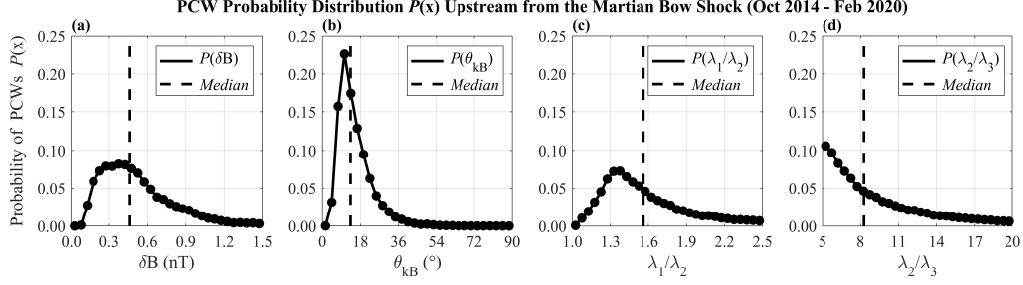


Figure 5. Probability distribution $P(x)$ of PCWs in the upstream region from October 2014 through February 2020 as a function of (a) δB , (b) θ_{kB} , (c) λ_1/λ_2 and (d) λ_2/λ_3 . The dashed vertical line represents the median value in each probability distribution.

399 wave amplitude δB , propagation angle θ_{kB} , λ_1/λ_2 , and λ_2/λ_3 are 0.05 nT, 3° , 0.05, and
 400 0.50, respectively. The PCW probability distribution for wave amplitude is shown in Fig-
 401 ure 5a, with a median amplitude of $\delta B = 0.46$ nT. $P(\delta B)$ reaches a maximum plateau
 402 for wave amplitudes $\delta B = 0.20$ nT – 0.55 nT. Figure 5b displays $P(\theta_{kB})$, with median
 403 and mode θ_{kB} values equal to 13.3° and 10.5° , respectively. The PCW probability dis-
 404 tribution for λ_1/λ_2 is presented in Figure 5c, with median and mode λ_1/λ_2 values equal
 405 to 1.56 and 1.35, respectively. Finally, a decreasing trend in $P(\lambda_2/\lambda_3)$ is displayed in Fig-
 406 ure 5d, with a median value of $\lambda_2/\lambda_3 = 8.28$.

407 Figure 6 presents the probability distribution function of PCWs, separated into the
 408 three HR and LR groups, for the same wave properties. The bin widths for each wave
 409 property are analogous to the sizes considered in Figure 5. The mode values of δB for
 410 the HR1, HR2, and HR3 probability distributions are 0.53 nT, 0.38 nT, and 0.23 nT,
 411 respectively. Indeed, we observe that the location of the peak in $P(\delta B)$ shifts to lower
 412 δB values for each consecutive Martian year near PH. Similarly, the median amplitude
 413 also decreases for each HR group, with median values of 0.65 nT, 0.52 nT, and 0.37 nT
 414 for HR1, HR2, and HR3, respectively. Moreover, we find a similar trend for the PCW
 415 probability distribution of normalized wave amplitude ($\delta B/B$), shown in Figure S1. Lower
 416 median amplitudes compared to HR are observed for the LR groups with δB around 0.35
 417 nT. $P(\theta_{kB})$ is almost identical for all HR groups, with median and mode θ_{kB} values around
 418 13.0° and 10.5° , respectively. More variation in the PCW probability distribution for θ_{kB}
 419 is found between the LR groups, with median θ_{kB} values closer to 21.0° . $P(\lambda_1/\lambda_2)$ tends
 420 to peak around 1.35 with a median λ_1/λ_2 value of about 1.55 for all HR groups, while

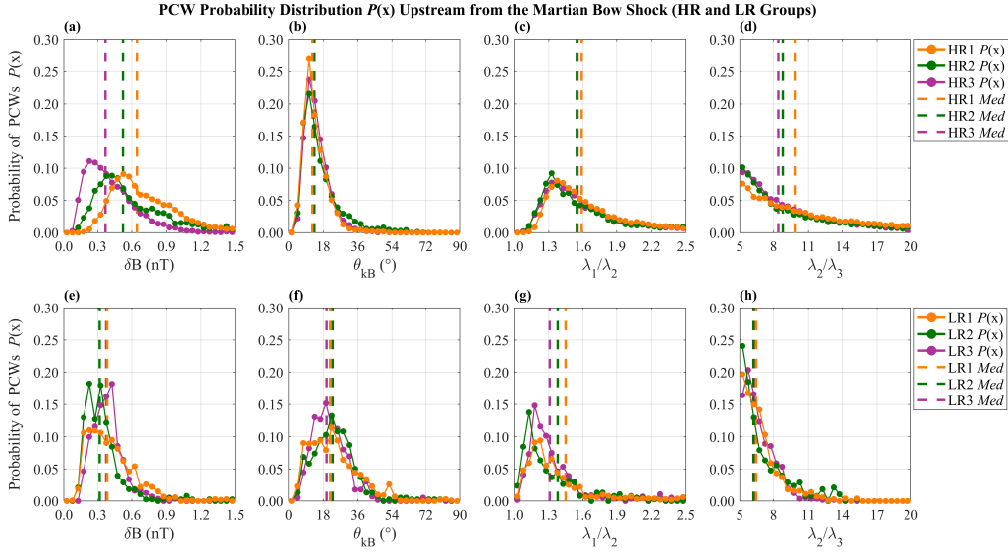


Figure 6. Probability distribution $P(x)$ of PCWs in the upstream region for HR1 (orange), HR2 (green), and HR3 (purple) as a function of (a) wave amplitude δB , (b) θ_{kB} , (c) λ_1/λ_2 and (d) λ_2/λ_3 . For the LR1 (orange), LR2 (green), and LR3 (purple) groups, the probability distribution $P(x)$ of PCWs as a function of (e) wave amplitude δB , (f) θ_{kB} , (g) λ_1/λ_2 and (h) λ_2/λ_3 . The dashed vertical line represents the median value in each probability distribution for HR and LR groups.

421 the LR distributions are centered closer to one. Finally, median values of λ_2/λ_3 in each
 422 HR probability distribution are constantly higher than the corresponding LR group.

423 The observed variability of the PCW median amplitude between HR groups can
 424 be due to several factors. As a result, next we study the relationship between median
 425 amplitude and MAVEN position. Figures 7a and 7b show the median amplitude of PCWs
 426 for the three HR groups as a function of X_{MSO} and altitude with bin sizes of $0.5R_M$ and
 427 $0.1R_M$, respectively. We consider bins with at least 100 events to compute the median
 428 PCW amplitude. All groups show a decreasing trend between the amplitude and the X_{MSO}
 429 coordinate. We also find that the median amplitudes of HR1 are greater than that of
 430 the other groups, whereas the smallest amplitudes are shown for HR3. Figure 7b also
 431 displays HR1 with larger median amplitudes than the other groups, while the smallest
 432 PCW amplitudes are found for HR3. Thus, Figure 7a would suggest that Mars is the
 433 source of these waves as the amplitude decreases with increasing distance from the planet,
 434 along the Mars-Sun axis. However, we do not find a similar monotonically decreasing

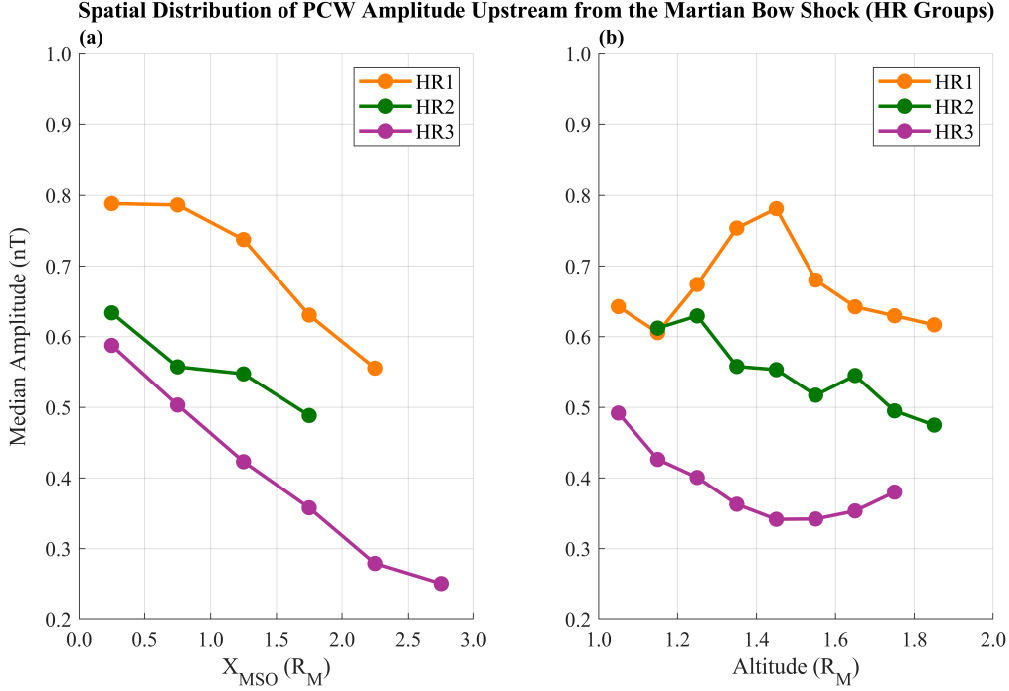


Figure 7. Median amplitude of upstream PCWs for the HR1 (orange), HR2 (green), and HR3 (purple) groups as a function of (a) X_{MSO} and (b) altitude.

435 trend between the median amplitude and altitude in all HR groups. This is also the case
 436 for analogous plots displaying the median wave amplitude as a function of the Y_{MSO} and
 437 Z_{MSO} coordinates, shown in Figure S2. It is worth mentioning that the decreasing trend
 438 in median amplitude when comparing these three Martian perihelion periods is observed
 439 for measurements inside and outside the foreshock of Mars, and also for the normalized
 440 wave amplitude ($\delta B/B$).

441 In addition, we analyze the relationship between PCW amplitude and IMF cone
 442 angle for each HR group, shown in Figure 8. The median amplitude is calculated for α
 443 bin sizes of 10° , with a range from about 0.2 nT to 1.2 nT. Similar to Figure 7a, the HR1
 444 curve has the largest amplitudes for all IMF cone angles, whereas the smallest median
 445 amplitudes are observed for HR3. A strong decreasing trend for median amplitude as
 446 a function of α is shown for HR1, while the magnitude of the slope, on average, decreases
 447 with each consecutive Martian year.

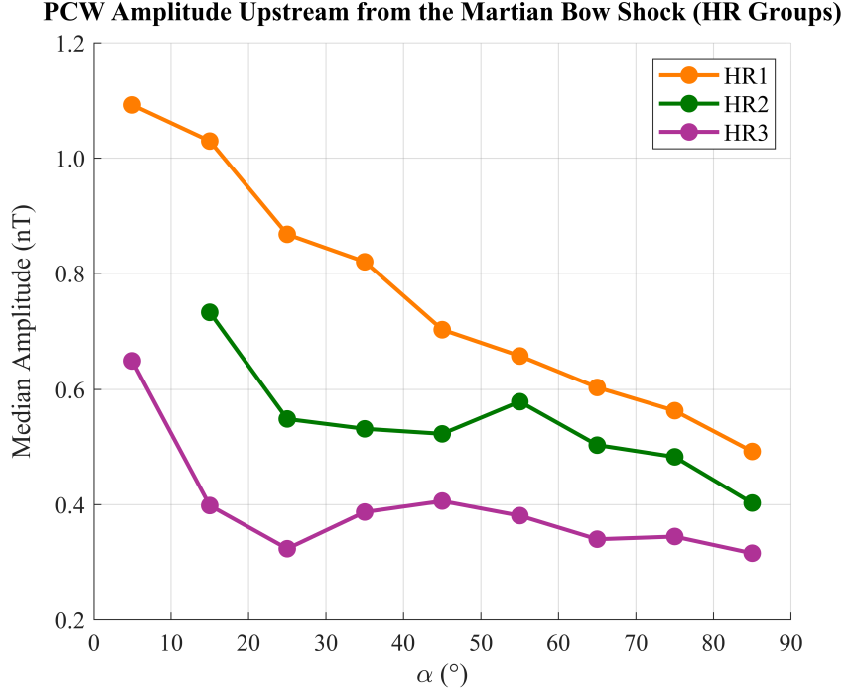


Figure 8. Median amplitude of PCWs in the upstream region for the HR1 (orange), HR2 (green), and HR3 (purple) groups as a function of IMF cone angle α .

4.3 Solar Wind Conditions Favoring PCW Generation

Figures 9a through 9e display histograms of the number of upstream 512 second time intervals as a function of IMF cone angle α , SW speed v_{SW} , Alfvén speed v_A , SW ion density n_{SW} , and SW proton flux $n_{SW}v_{SW}$, with bin sizes of 5° , 50 km s^{-1} , 10 km s^{-1} , 4.0 cm^{-3} , and $2.0 \times 10^8 \text{ cm}^2 \text{ s}^{-1}$, respectively. The Alfvén speed is computed with the SW proton density from SWIA, assuming the SW is composed of protons, and magnetic field measurements from the MAG instrument. Most of the upstream intervals are observed under $\alpha > 45^{\circ}$, $v_{SW} \sim 350 \text{ km s}^{-1}$, $v_A \sim 35 \text{ km s}^{-1}$, $n_{SW} < 4 \text{ cm}^{-3}$, and $n_{SW}v_{SW} \sim 10^8 \text{ cm}^2 \text{ s}^{-1}$. To compute the PCW occurrence rate, we consider bins with at least 100 upstream intervals for each histogram to ensure sufficient statistics.

Similar to Figure 3b, we calculate the PCW occurrence rate from the ratio of identified PCW events to the total number of upstream intervals within each bin for the SW parameters. As seen in Figure 9f, more PCWs occur for low to intermediate cone angles ($20^{\circ} < \alpha < 45^{\circ}$), with a distinct peak at 22.5° . A small peak between 50° and 60° is also apparent, very close to the Parker spiral angle of Mars ($\sim 55^{\circ}$). Figure 9g presents

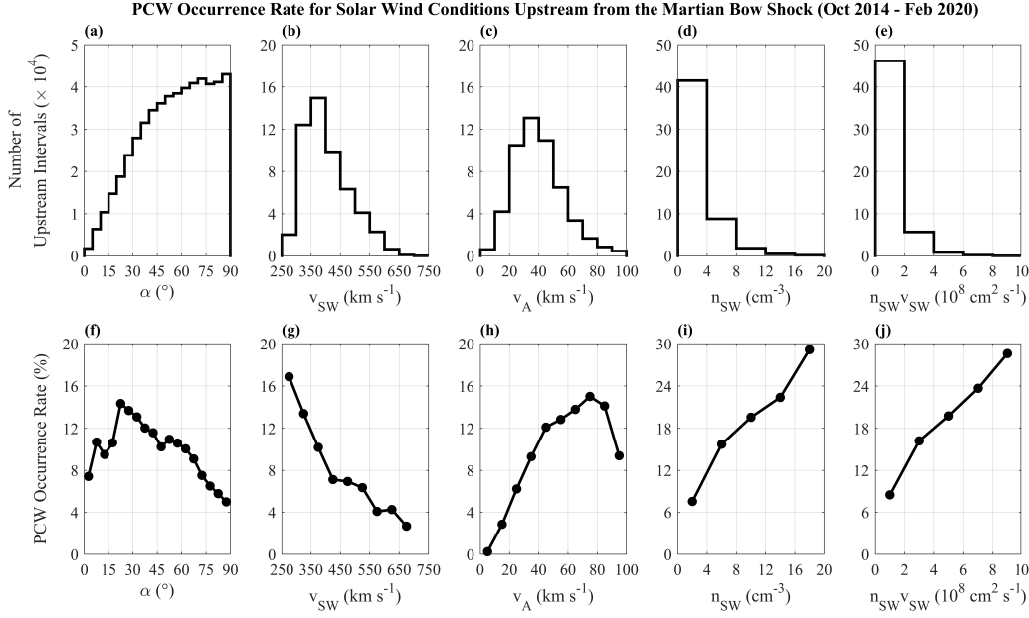


Figure 9. Histograms of the number of 512 second time intervals (in ten thousands) upstream from the Martian bow shock as a function of (a) IMF cone angle α , (b) SW speed v_{SW} , (c) Alfvén speed v_A , (d) SW density n_{SW} and (e) SW proton flux $n_{SW}v_{SW}$ between October 2014 through February 2020. PCW occurrence rate (%) as a function of (f) IMF cone angle α , (g) SW speed v_{SW} , (h) Alfvén speed v_A , (i) SW density n_{SW} and (j) SW proton flux $n_{SW}v_{SW}$.

463 a decreasing trend in PCW occurrence rate of about 14% with increasing SW speed. The
 464 occurrence rate increases for larger Alfvén speeds until a value of about 75 km s^{-1} , as
 465 shown in Figure 9h. Figures 9i and 9j display a similar increasing trend in PCW abun-
 466 dance as a function of both SW proton density and flux, respectively.

467 Figure 10 presents the PCW occurrence rate for the same SW parameters displayed
 468 in Figure 9, for each HR group. The LR groups are not shown as the PCW occurrence
 469 rate for each bin is too low ($< 1\%$) to determine any significant trends with the SW con-
 470 ditions. Figures 10a through 10e show the normalized number of upstream time inter-
 471 vals for each SW parameter. We find similar distributions for the IMF cone angle, SW
 472 proton density, and proton flux for all HR groups. The v_{SW} histogram for HR2 is cen-
 473 tered at slightly faster speeds and the v_A histogram for HR3 is centered at slightly slower
 474 speeds compared to the remaining HR groups. In Figure 10f, the HR1 group shows more
 475 PCWs for $20^\circ < \alpha < 45^\circ$, with a large peak at $\alpha \sim 22.5^\circ$. The PCW occurrence rate
 476 is maximized for IMF cone angles between 20° and 60° in the HR2 group. The occur-

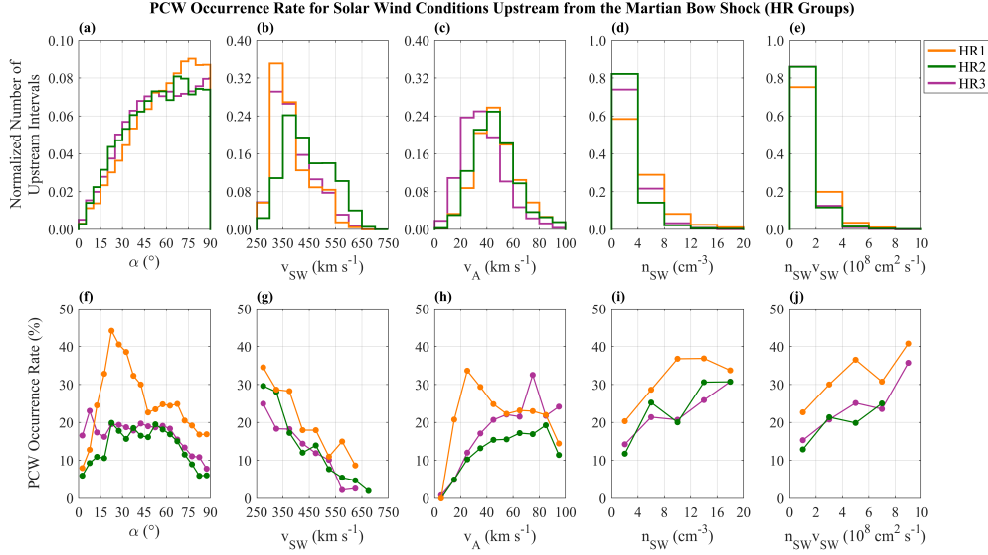


Figure 10. HR1 (orange), HR2 (green), and HR3 (purple) histograms of the normalized number of 512 second time intervals upstream from the Martian bow shock as a function of (a) IMF cone angle α , (b) SW speed v_{SW} , (c) Alfvén speed v_A , (d) SW density n_{SW} and (e) SW proton flux $n_{SW}v_{SW}$ between October 2014 through February 2020. PCW occurrence rate (%) for the HR1 (orange), HR2 (green), and HR3 (purple) groups as a function of (f) IMF cone angle α , (g) SW speed v_{SW} , (h) Alfvén speed v_A , (i) SW density n_{SW} and (j) SW proton flux $n_{SW}v_{SW}$.

477 rence rate for HR3 is approximately constant before dropping off around $\alpha = 60^\circ$. The
 478 PCW abundance in Figure 10g decreases for faster SW speeds among all HR groups. In
 479 Figure 10h, PCW occurrence rate for the HR2 and HR3 curves increases for faster Alfvén
 480 speeds up to 75 km s^{-1} . However, we do not observe a similar trend in HR1 for $v_A >$
 481 25 km s^{-1} . Figures 10i and 10j display an increasing trend in PCW abundance for both
 482 SW proton density and flux for all HR groups, respectively.

483 5 Discussion

484 We present a comprehensive study of PCWs utilizing both magnetic field and plasma
 485 observations from MAVEN, encompassing ~ 2.8 Martian years of data. This work ex-
 486 pands upon the analysis of Romanelli et al. (2016) based on MAVEN MAG and EUV
 487 measurements and numerical simulations, as well as the work by Romanelli et al. (2013)
 488 and Bertucci et al. (2013), based on MGS MAG data. These earlier studies suggested
 489 a long-term trend, on a timescale of about one Martian year, where PCWs are observed

490 more frequently near Martian perihelion. In this work, we confirm the presence of such
491 an annual trend, in which a gradual increase of about 30% – 35% in occurrence rate is
492 found near perihelion and northern winter solstice for each Martian year. In contrast,
493 rates of PCW occurrence remain below about 3% during time periods close to Martian
494 aphelion, agreeing with previous results.

495 A similar long-term trend was reported for the temporal variability of exospheric
496 H column density by Halekas (2017). Upstream H density is found to peak between so-
497 lar longitudes of 263° and 288°, in which densities observed near perihelion are an or-
498 der of magnitude larger compared to periods close to aphelion (Halekas, 2017). Slightly
499 offset from this L_s range, the three peaks in PCW occurrence rate, shown in Figure 3b,
500 occur between solar longitudes of 280° and 302°. This would indicate a time lag between
501 Martian perihelion, peak exospheric H density, and peak PCW abundance. Halekas (2017)
502 suggested the observed lag between perihelion and peak H density could be the result
503 of delayed upper atmospheric responses to solar inputs, or seasonal effects in combina-
504 tion with direct solar EUV flux influence. In this regard, simulated profiles of upper ex-
505 ospheric H densities in the upstream region between 10,000 km and 20,000 km have been
506 found to be more directly linked to changes in temperature at the exobase, dependent
507 on solar EUV fluxes (Chaufray et al., 2015; Romanelli et al., 2016). Daily irradiances
508 observed by the MAVEN Extreme Ultraviolet Monitor (EUVM) instrument (Eparvier
509 et al., 2015) also display a long-term temporal trend with increasing intensity for smaller
510 heliocentric distance (e.g., Romanelli et al., 2016; Thiemann et al., 2017), similar to the
511 timescale of exospheric H density variability. The ionization of more planetary particles
512 under denser exospheric H profiles near perihelion could then increase the newborn ion
513 population density, potentially providing more energy to increase the observed abundance
514 of PCWs. Interestingly, we identify an average delay of ~ 25 days between the H den-
515 sity peak and PCW occurrence rate peak. We also report an asymmetry between the
516 growth and decay phases of PCW abundance, as displayed in Figure 3b. Such features
517 are found for the three Martian years near each perihelion explored in this work, con-
518 sistent with previous observations (Romanelli et al., 2016). Possible causes for the ob-
519 served time lag and asymmetry are not currently understood, however such signatures
520 could be partly related to the seasonal sampling biases close to perihelion and NWS that
521 can be seen in Figures 3a and 3c.

522 Moreover, dust activity and atmospheric upwelling can have a significant role in
523 varying lower atmospheric water vapor concentration, influencing H exosphere variabil-
524 ity. This has been suggested by several studies, including work based on MAVEN, MEX,
525 and Hubble Space Telescope scattered Lyman α brightness observations (e.g., Bhattacharyya
526 et al., 2015, 2017, 2020; Chaffin et al., 2014; Clarke et al., 2014, 2017). Martian regional
527 dust storms have been observed to increase the near-surface atmospheric temperature
528 at 0.5 mbar by 15 K – 20 K, whereas planet-encircling dust storms can raise the tem-
529 perature by 30 K – 40 K, due to an increased opacity of the lower atmosphere (Smith,
530 2009). This effect can amplify atmospheric large scale circulation, allowing water vapor
531 near the Martian surface to freely mix up to higher thermospheric altitudes (Chaffin et
532 al., 2014). Therefore, initial large concentrations of water vapor high in the lower atmo-
533 sphere could affect the H exosphere (Aoki et al., 2019; Bhattacharyya et al., 2015; Chaf-
534 fin et al., 2017; Clarke et al., 2014; Fedorova et al., 2006, 2009, 2018, 2020; Heavens et
535 al., 2018; Maltagliati et al., 2011, 2013). For each Martian year, higher PCW occurrence
536 rates take place during part of the dust storm season, shown by the gray regions in Fig-
537 ure 3b. In this regard, it is worth mentioning that we observe a smaller secondary peak
538 ($\sim 20\%$) in the PCW occurrence rate between June and July 2018, two to three months
539 before the third Martian perihelion. In contrast, we do not find a similar secondary peak
540 greater than $\sim 15\%$ in occurrence rate a few months before perihelion for the other Mar-
541 tian years. The small peak of PCWs around July 2018 may be at least partly related
542 to the global dust storm of summer 2018, the first global event since 2007 (Sánchez-Lavega
543 et al., 2019). Global dust storms can occur from interactions between local and regional
544 dust storms that extend the growth duration of dust lifting and create new sites of dust
545 activity along the planet, distributing material almost completely around Mars within
546 a timescale of one to two weeks (Smith & Guzewich, 2019). The 2018 dust event became
547 a global scale storm by mid-June ($L_s \sim 193^\circ$) and continued until early July ($L_s \sim$
548 205°) before dust activity declined to normal levels for the perihelion season in mid-September
549 ($L_s \sim 250^\circ$), occurring close to the time interval when the small peak in Figure 3b is
550 observed (Guzewich et al., 2019). Additionally, we observe a small peak between Jan-
551 uary and March 2019 of about 7%, which could be linked to the early 2019 regional dust
552 storm from $L_s \sim 320^\circ$ to 340° (Aoki et al., 2019; Fedorova et al., 2020).

553 It is important to note that this periodic trend in PCW occurrence as a function
554 of time is present for various temporal bin sizes. Bin widths of 10 to 25 days with 1 day

555 increments were tested to ensure that the trend observed in PCW occurrence rate is in-
 556 dependent of bin size for weekly to monthly time scales. We selected 15 days to cover
 557 a sufficiently large temporal scale, similar to the time span of significant variations in
 558 observed planetary pick-up ion detection rate (Yamauchi et al., 2015). By displaying the
 559 PCW occurrence rate as a function of the Martian solar longitude (Figure 3c), we ob-
 560 serve that the overall trend shows a gradual increase of PCW occurrence rate until a peak
 561 slightly after perihelion and NWS. While the HR1 group contains more observations closer
 562 to perihelion than HR3, suggesting that seasonal biases might affect comparisons between
 563 HR periods, it is also important to emphasize that Y3 still presents 1,000 upstream in-
 564 tervals or more in each bin during these times. Although the HR2 group does not have
 565 observations during perihelion or NWS, the shape and timing of the PCW occurrence
 566 rate peak is consistent with the long term trend observed for the other two periods. In
 567 addition, different values were considered for the constants ξ_{\perp} , ξ_{\parallel} , and λ_{23} in the selec-
 568 tion criteria to identify variations in the occurrence rate. We find that PCW abundance
 569 is still maximized close to each perihelion in a Martian year for $\xi_{\perp} \geq 1.5$, $\xi_{\parallel} \geq 2$, and
 570 $\lambda_{23} \geq 5$, with smaller observed rates as these parameters are increased. Furthermore,
 571 we find that this annual trend cannot be associated with sampling biases based on the
 572 MSO spatial coverage of MAVEN. For example, we observe similar ranges of X_{MSO} for
 573 each Martian year between the HR and LR groups. MAVEN is also able to sample the
 574 northern and southern hemispheres during at least one HR and LR group throughout
 575 the three Martian years, suggesting the presence of the PCW occurrence rate peak is in-
 576 dependent of the sampling of this coordinate. Since most of the HR and LR groups dis-
 577 play similar distributions of SC altitude, and the altitude range covered by MAVEN is
 578 relatively small, our results indicate that the long-term trend cannot be associated from
 579 sampling biases in radial distance near Mars. We also find that this trend is still present
 580 when the analysis is restricted to measurements inside or outside of the Martian fore-
 581 shock. Moreover, Romanelli et al. (2016) did not report the increase in PCW occurrence
 582 rate to be associated with variations in the angle between the SW and background mag-
 583 netic field direction for the first Martian year. We confirm this result for the following
 584 two Martian years by comparing the IMF cone angle distributions for the HR and LR
 585 groups.

586 We also analyzed PCW wave properties as seen by MAVEN. We find that these
 587 waves have mainly moderate to large amplitudes (~ 0.1 nT to 1.0 nT), slightly larger

588 than the range observed by Brain et al. (2002). More PCWs in both HR and LR groups
589 are observed in the $\theta_{kB} = 10^\circ - 25^\circ$ range, suggesting that these waves propagate quasi-
590 parallel to \mathbf{B} , agreeing with results from Romanelli et al. (2013), without displaying a
591 significant change with Martian heliocentric distance. The PCW distribution as a func-
592 tion of λ_1/λ_2 peaks at 1.35, indicating that these waves are primarily elliptical. The tail
593 of $P(\lambda_1/\lambda_2)$ for relatively large λ_1/λ_2 values may be attributed to time intervals with
594 solar wind discontinuities and not highly elliptical waves. However, we have checked that
595 these events do not significantly affect the results presented in this study. Indeed, the
596 number of events with $\lambda_1/\lambda_2 > 5$ account for less than 4% of the upstream intervals
597 identified with PCWs. The LR distribution for PCW abundance is maximized at lower
598 λ_1/λ_2 values compared to the corresponding HR groups. Thus, we find that these waves
599 are closer to being circularly polarized for periods near Martian aphelion than perihe-
600 lion. This difference could be associated with variations in the growth phase of waves
601 at the observation time due, in turn, to changes in the linear wave growth rate as sev-
602 eral SW and planetary properties vary between the HR and LR groups. Our study sug-
603 gests that LR groups are characterized by low PCW occurrence rates, relatively low wave
604 amplitudes and approximately circular polarization. Additionally, we report that PCWs
605 in HR groups are closer to being planar than those observed in LR groups, based on the
606 probability distributions as a function of λ_2/λ_3 . Regardless of the group, we find that
607 PCWs are left-hand polarized in the spacecraft frame.

608 In addition, we report PCW amplitude to decrease with distance along the X_{MSO}
609 axis for all HR groups, shown in Figure 7a, suggesting that Mars is the source of these
610 waves. This trend is consistent with the result reported by Halekas et al. (2020) based
611 on MAVEN observations. In contrast, Figure 7b shows the HR amplitude curves do not
612 necessarily decrease with larger altitudes from Mars. In agreement with our results, sig-
613 nificant amplitude variations with altitude are not found with MAVEN data from Oc-
614 tober 2014 to November 2018 (Liu et al., 2020), whereas previous studies with MGS data
615 have observed wave amplitudes to slowly decrease with radial distance from Mars (Brain
616 et al., 2002; Romanelli et al., 2013; Wei & Russell, 2006; Wei et al., 2014). Such differ-
617 ences between results from the MAVEN and MGS missions may be attributed to differ-
618 ent combinations of multiple SW and planetary properties influencing PCW amplitude
619 during each Martian year, such as pick-up ion rates, pick-up velocity, pick-up geometry,
620 and wave growth time (Wei et al., 2014). Moreover, it is worth emphasizing the differ-

621 ence in altitude range covered by MGS premapping orbits (up to $\sim 15R_M$) and MAVEN's
622 orbital trajectory. Future studies could analyze the relation between observed amplitude
623 and radial distance from Mars based on these factors, combining spacecraft observations
624 and numerical simulations.

625 Furthermore, we find a decrease in median and mode wave amplitudes by ~ 0.15
626 nT for each consecutive HR group. This result is not likely attributed to sampling bi-
627 ases in MSO spatial coverage, based on the relationship between wave amplitude and dis-
628 tance from the Martian bow shock. Each HR group covers a similar range in X_{MSO} and
629 altitude. The decline of PCW amplitude for each Martian year is present for all mea-
630 sured X_{MSO} and altitude values within the spatial range of MAVEN. Analogous results
631 are also found for the Y_{MSO} and Z_{MSO} coordinates, shown in Figure S2. Additionally,
632 we do not observe significant differences in the distributions of SW conditions between
633 HR groups, displayed in Figures 10a through 10e, that could be related to this trend.
634 This analysis suggests the reduction in amplitude could be associated with foreshock bi-
635 ases (Mazelle et al., 2018; Meziane et al., 2017), asymmetries due to the SW convective
636 electric field influencing newborn protons (Wei & Russell, 2006), or changes in the Mar-
637 tian atmospheric response to variability in several solar inputs and/or solar cycle effects.
638 For instance, the photoionization frequency of exospheric H^+ near Mars can increase by
639 a factor of 2, from solar minimum to solar maximum (Modolo et al., 2005).

640 A decreasing trend between the wave amplitude and IMF cone angle is also found
641 for the HR1 group in this study. In contrast, we do not observe such strong decreasing
642 trend for the HR2 and HR3 groups in Figure 8. Previous studies based on MGS and MAVEN
643 measurements have observed an amplitude dependence on the IMF cone angle (Liu et
644 al., 2020; Romanelli et al., 2013). This relationship has also been studied with numer-
645 ical one-dimensional hybrid simulations of the Martian planetary environment by Cowee
646 et al. (2012), indicating that saturation wave energy decreases for larger cone angles for
647 an estimated ion production rate of $\Lambda = 3.4 \times 10^{-4} \text{ cm}^{-3} \text{ s}^{-1}$. However, Wei et al. (2014)
648 did not find such dependence on α analyzing MGS MAG measurements from the first
649 aerobraking phase of the mission, in agreement with our observations for the HR2 and
650 HR3 groups. One possible explanation for this potential disagreement between the HR
651 groups can be derived from the results by Cowee et al. (2012). As suggested in the study,
652 PCWs observed upstream from the Martian bow shock are not likely to be completely
653 saturated. For instance, PCWs must travel at least for 10 cyclotron periods to reach wave

654 saturation, assuming $\alpha = 0^\circ$ (Cowee et al., 2012). If we consider a typical wave frequency
 655 of $f \sim 0.06$ Hz and SW velocity of $v_{SW} \sim 400$ km s⁻¹, the wave will be convected over
 656 a distance of $\sim 20R_M$ before achieving saturation. Therefore, PCWs with higher wave
 657 frequencies could reach saturation in shorter distances with respect to Mars. Indeed, if
 658 we restrict this analysis to wave frequencies greater than 0.07 Hz, we obtain similar fre-
 659 quency distributions for the HR groups, focusing on waves that are more likely to have
 660 reached saturation. After applying this constraint, we find all three curves to display a
 661 strong decreasing trend in amplitude with similar slopes, displayed in Figure S3. Con-
 662 sequently, our analysis suggests that variations in the measured wave frequency distri-
 663 butions between HR groups could be related to the different trends shown in Figure 8
 664 for each Martian year, possibly explaining the disagreement between results reported in
 665 previous studies.

666 We have also analyzed the relationship between several SW conditions and the pres-
 667 ence of these waves. The PCW occurrence rate as a function of IMF cone angle reveals
 668 that more waves are detected for low to intermediate cone angles ($20^\circ < \alpha < 45^\circ$), in
 669 agreement with Liu et al. (2020), Romanelli et al. (2013) and Wei et al. (2014). This is
 670 observed for HR1 and HR2, whereas high PCW abundance in HR3 occurs for a slightly
 671 larger range ($0^\circ < \alpha < 60^\circ$). The latter result for the HR3 distribution does not sig-
 672 nificantly change if we disregard MAVEN data from 20 July 2018 through 15 Septem-
 673 ber 2018 (corresponding to the 2018 global dust storm duration) in our analysis. The
 674 peak near $\alpha = 22.5^\circ$ in Figure 9f is mainly attributed from HR1, as can be seen from
 675 Figure 10f. This difference could be partly due to effects related to seasonal sampling
 676 biases near perihelion and NWS. For example, the value of the PCW occurrence rate peak
 677 in Figure 10f for HR1, and therefore in Figure 9f, can vary depending on the range of
 678 magnetic field intensity selected. For instance, we find better agreement between the dis-
 679 tributions when the analysis is restricted to cases with $B \geq 4$ nT, where each Martian
 680 year displays a peak in PCW occurrence rate around $\alpha = 22.5^\circ$. However, it is impor-
 681 tant to emphasize that despite of this variability, higher rates of PCW occurrence are
 682 consistently observed for IMF cone angles below 45° . As previously reported by Liu et
 683 al. (2020), an explanation for the preference for low to intermediate IMF cone angles could
 684 be the result of a trade-off between associated saturation wave energy, characteristic growth
 685 time and newborn planetary proton density. For instance, the ion-ion RH instability that
 686 is often the most easily excited mode for $\alpha < \sim 75^\circ$ is characterized by relatively large

687 saturation wave amplitudes and long growth times, but does not require high pick-up
688 ion density when compared with the resonant plasma instability present at large IMF
689 cone angles (Cowee et al., 2012; Liu et al., 2020). Therefore, the observed PCW occur-
690 rence rate peak for low to intermediate IMF cone angles could be the net result of dif-
691 ferent growth times and threshold planetary ion densities for the dominant plasma in-
692 stability under a given IMF cone angle range.

693 PCWs are additionally observed for slower SW speeds ($v_{SW} < 400 \text{ km s}^{-1}$), with
694 a decreasing trend in occurrence rate for faster speeds. This is consistently seen for all
695 HR groups and the entire span of available MAVEN data, confirming the results from
696 Halekas et al. (2020) between September through November 2018. Although this trend
697 disagrees with linear wave growth theory (Gary et al., 1986), Delva et al. (2015) also re-
698 ported a similar case for PCWs near Venus from the Venus Express mission. Delva et
699 al. (2015) associated this result with a larger transit time for newborn planetary protons
700 to interact with the SW, contributing to the growing instability responsible for the pres-
701 ence of PCWs. This effect observed near Venus may also be the reason for increased PCW
702 abundance during slower SW speed conditions near Mars. In addition, we do not find
703 a significant relationship between PCW occurrence rate and Alfvén speed. Figure 9h dis-
704 plays a slight preference for $40 \text{ km s}^{-1} < v_A < 80 \text{ km s}^{-1}$, however, Figure 10h shows
705 a slightly opposite trend between HR1 and the other two HR groups. This discrepancy
706 can be partly explained by seasonal sampling biases, which cause MAVEN to observe
707 different PCW distributions of magnetic field intensity and SW density each Martian year,
708 which directly affect Alfvén speed. Interestingly, as in the case for the PCW occurrence
709 rate as a function of the IMF cone angle, when restricting the analysis to cases with $B \geq$
710 4 nT we observe an overall decreasing trend in occurrence rate for faster Alfvén speeds
711 greater than 40 km s^{-1} for all Martian years, similar to the HR1 curve in Figure 10h.
712 Thus, this analysis suggests that the identified discrepancy could be partly attributed
713 to sampling biases in the magnetic field intensity due, in turn, to MAVEN sampling of
714 the upstream region during each Martian year. A deeper study of this dependence is be-
715 yond the scope of this study.

716 As shown in Figure 10i, we find higher PCW occurrence rates for larger SW pro-
717 ton densities for all HR groups. Thus, this trend also confirms the result initially reported
718 by Halekas et al. (2020). This relationship does not seem to be in agreement with lin-
719 ear theory for most of the cases associated with the RH instability in the cool beam regime.

720 Indeed, in these cases, the linear wave growth rate is expected to be proportional to the
721 ratio of planetary ion density to the SW particle density (n_i/n_{SW}), therefore suggest-
722 ing that more PCWs should be present for lower SW densities (Gary, 1991). However,
723 an increase in the SW density gives rise to an increase in the charge exchange ionization
724 frequency of the Martian H exosphere, which is linearly proportional to both SW speed
725 and density (M. H. G. Zhang et al., 1993). Thus, despite the fact that higher SW den-
726 sities reduce the expected linear wave growth rate, the same increase can give rise to higher
727 newborn ion densities due to charge exchange, providing an explanation for the observed
728 trend. In agreement with this interpretation, Rahmati et al. (2018) reported that charge
729 exchange is the leading ionization mechanism of exospheric H atoms upstream from Mars,
730 with an ionization frequency larger compared to that of photoionization and electron im-
731 pact ionization processes.

732 Finally, our results allow us to provide estimates for the expected pitch angle range
733 around which charged particles interacting with PCWs can be trapped near Mars, fol-
734 lowing the theoretical work by Mazelle et al. (2000), Mazelle et al. (2003), and Romanelli
735 et al. (2018). $P(\delta B/B)$ is maximized for a normalized wave amplitude $\delta B/B \sim 0.1$,
736 shown in Figure S1. In addition, PCWs with this normalized amplitude are observed more
737 frequently for an IMF cone angle range between $\alpha = 20^\circ$ and the Parker spiral angle
738 ($\sim 55^\circ$). As shown in Romanelli et al. (2018), these derived properties suggest PCWs
739 that might arise from proton ring-beam distributions will tend to trap particles with ap-
740 proximately the same energy (in the wave rest frame) close to a pitch angle range be-
741 tween 40° and 60° . Future studies could test this prediction utilizing velocity distribu-
742 tion functions measured by SWIA.

743 6 Conclusions

744 This paper presents a statistical study with MAVEN magnetic field and plasma ob-
745 servations from October 2014 through February 2020 to analyze the temporal variabil-
746 ity of PCW occurrence for about three Martian years. We confirm that PCWs tend to
747 occur more frequently near each Martian perihelion and northern winter solstice. Our
748 results suggest this long-term trend is associated with changes in the Martian heliocen-
749 tric distance, likely due to variations in the H exosphere density and also possibly related
750 to changes in water vapor concentrations in the lower and upper atmosphere influenced
751 by dust activity. In particular, this variability does not seem to be related to biases in

752 MAVEN spatial coverage, length of temporal binning, or the considered PCW selection
753 criteria.

754 We also find that the observed PCWs propagate mostly quasi-parallel to the mean
755 magnetic field direction, with amplitudes ranging from 0.1 nT to 1.0 nT, and are pla-
756 nar and elliptically left-hand polarized in the spacecraft reference frame. Our results sug-
757 gest that the reduction in median amplitude between each Martian year cannot be at-
758 tributed to the spatial coverage of each MSO coordinate nor differences in distributions
759 of SW conditions. Such decrease could be associated with physical processes taking place
760 in the Martian foreshock, the SW convective field influence on newborn protons, and/or
761 temporal changes in solar inputs over these timescales. Finally, we observe these waves
762 more frequently for low to intermediate IMF cone angles ($20^\circ < \alpha < 45^\circ$), slower SW
763 speeds ($v_{SW} < 400 \text{ km s}^{-1}$), and higher SW proton densities ($n_{SW} > 5 \text{ cm}^{-3}$). As pre-
764 viously reported by Liu et al. (2020), the preference for this IMF cone angle range is likely
765 the result of the trade-off between associated linear wave growth rates, wave saturation
766 energies, and pick-up proton densities. Furthermore, while the PCW occurrence rate de-
767 pendence on the SW speed seems to disagree with linear theory, this outcome could be
768 associated with larger transit times for planetary pick-up protons to interact with the
769 SW flow. In addition, the observed dependence on SW density suggests that an increase
770 in the ionization frequency of H atoms by charge exchange is responsible for an increase
771 in the newborn proton density, and therefore in the linear wave growth rate.

772 Future studies could be focused on the analysis of the observed temporal lag be-
773 tween Martian perihelion, peak exospheric H density, and peak PCW occurrence rate
774 upstream from Mars. Such work would improve the current understanding on the rela-
775 tionship between exospheric H density and the generation of these upstream low frequency
776 waves. In particular, confining the timescales of these phenomena, in addition to ana-
777 lyzing other related solar and planetary properties, could allow us to better understand
778 the physical processes coupling the Martian atmosphere with the plasma environment.

779 Acknowledgments

780 The MAVEN mission is supported by NASA through the Mars Scout program. O. M.
781 R. is supported by CRESST II (Center for Research and Exploration in Space Sciences
782 & Technology) and the University of Maryland, College Park. N. R. is an Assistant Re-
783 search Scientist at NASA Goddard Space Flight Center and the University of Maryland,

784 Baltimore County hired through a cooperative agreement with CRESST II. The work
 785 by C. M. is also supported by the French Space Agency CNES. MAVEN data are pub-
 786 licly available through the Planetary Data System (<https://pds-ppi.igpp.ucla.edu/index.jsp>).

787 References

- 788 Acuña, M. H., Connerney, J. E. P., Wasilewski, P., Lin, R. P., Anderson, K. A.,
 789 Carlson, C. W., ... Ness, N. F. (1998). Magnetic field and plasma observa-
 790 tions at mars: Initial results of the mars global surveyor mission. *Science*,
 791 *279*(5357), 1676–1680. doi: 10.1126/science.279.5357.1676
- 792 Albee, A. L., Arvidson, R. E., Palluconi, F., & Thorpe, T. (2001). Overview of
 793 the mars global surveyor mission. *Journal of Geophysical Research: Planets*,
 794 *106*(E10), 23291–23316. doi: 10.1029/2000JE001306
- 795 Andrés, N., Romanelli, N., Hadid, L. Z., Sahraoui, F., DiBraccio, G., & Halekas, J.
 796 (2020). Solar wind turbulence around mars: Relation between the energy cas-
 797 cade rate and the proton cyclotron waves activity. *The Astrophysical Journal*,
 798 *902*(2), 134. doi: 10.3847/1538-4357/abb5a7
- 799 Aoki, S., Vandaele, A. C., Daerden, F., Villanueva, G. L., Liuzzi, G., Thomas, I. R.,
 800 ... LopezMoreno, J. (2019). Water vapor vertical profiles on mars in dust
 801 storms observed by tgo/nomad. *Journal of Geophysical Research: Planets*,
 802 *124*(12), 3482–3497. doi: 10.1029/2019JE006109
- 803 Bertucci, C., Romanelli, N., Chaufray, J.-Y., Gomez, D., Mazelle, C., Delva, M.,
 804 ... Brain, D. A. (2013). Temporal variability of waves at the proton cy-
 805 clotron frequency upstream from mars: Implications for mars distant hy-
 806 drogen exosphere. *Geophysical Research Letters*, *40*(15), 3809–3813. doi:
 807 10.1002/grl.50709
- 808 Bhattacharyya, D., Chaufray, J. Y., Mayyasi, M., Clarke, J. T., Stone, S., Yelle,
 809 R. V., ... Schneider, N. M. (2020). Two-dimensional model for the martian
 810 exosphere: Applications to hydrogen and deuterium lyman α observations.
 811 *Icarus*, *339*, 113573. doi: 10.1016/j.icarus.2019.113573
- 812 Bhattacharyya, D., Clarke, J. T., Bertaux, J.-L., Chaufray, J.-Y., & Mayyasi, M.
 813 (2015). A strong seasonal dependence in the martian hydrogen exosphere. *Geo-*
 814 *physical Research Letters*, *42*(20), 8678–8685. doi: 10.1002/2015GL065804
- 815 Bhattacharyya, D., Clarke, J. T., Chaufray, J.-Y., Mayyasi, M., Bertaux, J.-L.,

- 816 Chaffin, M. S., ... Villanueva, G. L. (2017). Seasonal changes in hydrogen es-
817 cape from mars through analysis of hst observations of the martian exosphere
818 near perihelion. *Journal of Geophysical Research: Space Physics*, *122*(11),
819 11,756–11,764. doi: 10.1002/2017JA024572
- 820 Brain, D. A., Bagenal, F., Acua, M. H., Connerney, J. E. P., Crider, D. H., Mazelle,
821 C., ... Ness, N. F. (2002). Observations of low-frequency electromagnetic
822 plasma waves upstream from the martian shock. *Journal of Geophysical Re-*
823 *search: Space Physics*, *107*(A6), 1076. doi: 10.1029/2000JA000416
- 824 Brinca, A. (1991). Cometary linear instabilities: from profusion to perspec-
825 tive. In A. D. Johnstone (Ed.), *Cometary plasma processes* (Vol. 61, pp.
826 211–221). Washington, D.C.: American Geophysical Union (AGU). doi:
827 10.1029/GM061p0211
- 828 Brinca, A., & Tsurutani, B. T. (1989). Influence of multiple ion species on low-
829 frequency electromagnetic wave instabilities. *Journal of Geophysical Research:*
830 *Space Physics*, *94*(A10), 13565–13569. doi: 10.1029/JA094iA10p13565
- 831 Chaffin, M. S., Chaufray, J.-Y., Deighan, J., Schneider, N. M., McClintock, W. E.,
832 Stewart, A. I. F., ... Jakosky, B. M. (2015). Three-dimensional structure in
833 the mars h corona revealed by iuvs on maven. *Geophysical Research Letters*,
834 *42*(21), 9001–9008. doi: 10.1002/2015GL065287
- 835 Chaffin, M. S., Chaufray, J.-Y., Stewart, I., Montmessin, F., Schneider, N. M., &
836 Bertaux, J.-L. (2014). Unexpected variability of martian hydrogen escape.
837 *Geophysical Research Letters*, *41*(2), 314–320. doi: 10.1002/2013GL058578
- 838 Chaffin, M. S., Deighan, J., Schneider, N. M., & Stewart, A. I. F. (2017). Elevated
839 atmospheric escape of atomic hydrogen from mars induced by high-altitude
840 water. *Nature Geoscience*, *10*(3), 174–178. doi: 10.1038/ngeo2887
- 841 Chaufray, J.-Y., Bertaux, J.-L., Leblanc, F., & Quémerais, E. (2008). Observation
842 of the hydrogen corona with spicam on mars express. *Icarus*, *195*(2), 598–613.
843 doi: 10.1016/j.icarus.2008.01.009
- 844 Chaufray, J.-Y., Gonzalez-Galindo, F., Forget, F., Lopez-Valverde, M. A., Leblanc,
845 F., Modolo, R., & Hess, S. (2015). Variability of the hydrogen in the mar-
846 tian upper atmosphere as simulated by a 3d atmosphere–exosphere coupling.
847 *Icarus*, *245*, 282–294. doi: 10.1016/j.icarus.2014.08.038
- 848 Clarke, J. T., Bertaux, J.-L., Chaufray, J.-Y., Gladstone, G. R., Quémerais, E.,

- 849 Wilson, J. K., & Bhattacharyya, D. (2014). A rapid decrease of the hydro-
850 gen corona of mars. *Geophysical Research Letters*, *41*(22), 8013–8020. doi:
851 10.1002/2014GL061803
- 852 Clarke, J. T., Mayyasi, M., Bhattacharyya, D., Schneider, N. M., McClintock, W. E.,
853 Deighan, J. I., ... Jakosky, B. M. (2017). Variability of d and h in the
854 martian upper atmosphere observed with the maven iuvs echelle channel.
855 *Journal of Geophysical Research: Space Physics*, *122*(2), 2336–2344. doi:
856 10.1002/2016JA023479
- 857 Connerney, J. E. P., Espley, J., Lawton, P., Murphy, S., Odom, J., Oliverson, R., &
858 Sheppard, D. (2015b). The maven magnetic field investigation. *Space Science*
859 *Reviews*, *195*(1–4), 257–291. doi: 10.1007/s11214-015-0169-4
- 860 Connerney, J. E. P., Espley, J. R., DiBraccio, G. A., Gruesbeck, J. R., Oliverson,
861 R. J., Mitchell, D. L., ... Jakosky, B. M. (2015a). First results of the maven
862 magnetic field investigation. *Geophysical Research Letters*, *42*(21), 8819–8827.
863 doi: 10.1002/2015GL065366
- 864 Cowee, M. M., Gary, S. P., & Wei, H. Y. (2012). Pickup ions and ion cyclotron wave
865 amplitudes upstream of mars: First results from the 1d hybrid simulation.
866 *Geophysical Research Letters*, *39*(8). doi: 10.1029/2012GL051313
- 867 Delva, M., Bertucci, C., Volwerk, M., Lundin, R., Mazelle, C., & Romanelli, N.
868 (2015). Upstream proton cyclotron waves at venus near solar maximum.
869 *Journal of Geophysical Research: Space Physics*, *120*(1), 344–354. doi:
870 10.1002/2014JA020318
- 871 Eparvier, F. G., Chamberlin, P. C., Woods, T. N., & Thiemann, E. M. B. (2015).
872 The solar extreme ultraviolet monitor for maven. *Space Science Reviews*,
873 *195*(1–4), 293–301. doi: 10.1007/s11214-015-0195-2
- 874 Fedorova, A. A., Bertaux, J.-L., Betsis, D., Montmessin, F., Korablev, O., Mal-
875 tagliati, L., & Clarke, J. (2018). Water vapor in the middle atmosphere
876 of mars during the 2007 global dust storm. *Icarus*, *300*, 440–457. doi:
877 10.1016/j.icarus.2017.09.025
- 878 Fedorova, A. A., Korablev, O. I., Bertaux, J.-L., Rodin, A. V., Kiselev, A., & Per-
879 rier, S. (2006). Mars water vapor abundance from spicam ir spectrometer:
880 Seasonal and geographic distributions. *Journal of Geophysical Research: Plan-*
881 *ets*, *111*(E9). doi: 10.1029/2006JE002695

- 882 Fedorova, A. A., Korablev, O. I., Bertaux, J.-L., Rodin, A. V., Montmessin, F.,
 883 Belyaev, D. A., & Reberac, A. (2009). Solar infrared occultation observations
 884 by spicam experiment on mars-express: Simultaneous measurements of the
 885 vertical distributions of h₂o, co₂ and aerosol. *Icarus*, *200*(1), 96–117. doi:
 886 10.1016/j.icarus.2008.11.006
- 887 Fedorova, A. A., Montmessin, F., Korablev, O., Luginin, M., Trokhimovskiy, A.,
 888 Belyaev, D. A., . . . Wilson, C. F. (2020). Stormy water on mars: The distri-
 889 bution and saturation of atmospheric water during the dusty season. *Science*,
 890 *367*(6475), 297–300. doi: 10.1126/science.aay9522
- 891 Gary, S. P. (1991). Electromagnetic ion/ion instabilities and their consequences in
 892 space plasmas: A review. *Space Science Reviews*, *56*(3–4), 373–415. doi: 10
 893 .1007/BF00196632
- 894 Gary, S. P. (1993). *Theory of space plasma microinstabilities* (No. 7). Cambridge:
 895 Cambridge University Press. doi: 10.1017/CBO9780511551512
- 896 Gary, S. P., & Madland, C. D. (1988). Electromagnetic ion instabilities in a
 897 cometary environment. *Journal of Geophysical Research: Space Physics*,
 898 *93*(A1), 235–241. doi: 10.1029/JA093iA01p00235
- 899 Gary, S. P., Madland, C. D., Schriver, D., & Winske, D. (1986). Computer simula-
 900 tions of electromagnetic cool ion beam instabilities. *Journal of Geophysical Re-
 901 search: Space Physics*, *91*(A4), 4188–4200. doi: 10.1029/JA091iA04p04188
- 902 Gruesbeck, J. R., Espley, J. R., Connerney, J. E. P., DiBraccio, G. A., Soobiah,
 903 Y. I., Brain, D., . . . Mitchell, D. L. (2018). The three-dimensional bow
 904 shock of mars as observed by maven. *Journal of Geophysical Research: Space
 905 Physics*, *123*(6), 4542–4555. doi: 10.1029/2018JA025366
- 906 Guzewich, S. D., Lemmon, M., Smith, C. L., Martínez, G., de Vicente-Retortillo,
 907 Á., Newman, C. E., . . . Zorzano Mier, M.-P. (2019). Mars science laboratory
 908 observations of the 2018/mars year 34 global dust storm. *Geophysical Research
 909 Letters*, *46*(1), 71–79. doi: 10.1029/2018GL080839
- 910 Halekas, J. S. (2017). Seasonal variability of the hydrogen exosphere of
 911 mars. *Journal of Geophysical Research: Planets*, *122*(5), 901–911. doi:
 912 10.1002/2017JE005306
- 913 Halekas, J. S., Ruhunusiri, S., Vaisberg, O. L., Harada, Y., Espley, J., Mitchell,
 914 D. L., . . . Brain, D. A. (2020). Properties of plasma waves observed up-

915 stream from mars. *Journal of Geophysical Research: Space Physics*, 125(9),
916 e2020JA028221. doi: 10.1029/2020JA028221

917 Halekas, J. S., Taylor, E. R., Dalton, G., Johnson, G., Curtis, D. W., McFadden,
918 J. P., ... Jakosky, B. M. (2015). The solar wind ion analyzer for maven. *Space*
919 *Science Reviews*, 195(1–4), 125–151. doi: 10.1007/s11214-013-0029-z

920 Heavens, N. G., Kleinböhl, A., Chaffin, M. S., Halekas, J. S., Kass, D. M., Hayne,
921 P. O., ... Schofield, J. T. (2018). Hydrogen escape from mars enhanced
922 by deep convection in dust storms. *Nature Astronomy*, 2(2), 126–132. doi:
923 10.1038/s41550-017-0353-4

924 Jakosky, B. M., Lin, R. P., Grebowsky, J. M., Luhmann, J. G., Mitchell, D. F.,
925 Beutelschies, G., ... others (2015). The mars atmosphere and volatile
926 evolution (maven) mission. *Space Science Reviews*, 195(1–4), 3–48. doi:
927 10.1007/s11214-015-0139-x

928 Lee, M. A. (1989). Ultralow frequency waves at comets. In B. T. Tsurutani &
929 H. Oya (Eds.), *Plasma waves and instabilities at comets and in magneto-*
930 *spheres* (Vol. 53, pp. 13–29). Washington, D.C.: American Geophysical Union
931 (AGU). doi: 10.1029/GM053p0013

932 Liu, D., Yao, Z., Wei, Y., Rong, Z., Shan, L., Arnaud, S., ... Wan, W. (2020). Up-
933 stream proton cyclotron waves: occurrence and amplitude dependence on imf
934 cone angle at mars from maven observations. *Earth and Planetary Physics*,
935 4(1), 51–61. doi: 10.26464/epp2020002

936 Maltagliati, L., Montmessin, F., Fedorova, A., Korablev, O., Forget, F., & Bertaux,
937 J.-L. (2011). Evidence of water vapor in excess of saturation in the atmosphere
938 of mars. *Science*, 333(6051), 1868–1871. doi: 10.1126/science.1207957

939 Maltagliati, L., Montmessin, F., Korablev, O., Fedorova, A., Forget, F., Mt-
940 tnen, A., ... Bertaux, J.-L. (2013). Annual survey of water vapor verti-
941 cal distribution and water aerosol coupling in the martian atmosphere ob-
942 served by spicam/mex solar occultations. *Icarus*, 223(2), 942–962. doi:
943 h10.1016/j.icarus.2012.12.012

944 Mazelle, C., Le Quéau, D., & Meziane, K. (2000). Nonlinear wave-particle interac-
945 tion upstream from the earth's bow shock. *Nonlinear Processes in Geophysics*,
946 7(3/4), 185–190. doi: 10.5194/npg-7-185-2000

947 Mazelle, C., Meziane, K., LeQuau, D., Wilber, M., Eastwood, J. P., Rme, H.,

- 948 ... Balogh, A. (2003). Production of gyrating ions from nonlinear wave-
949 particle interaction upstream from the earth's bow shock: A case study
950 from cluster-cis. *Planetary and Space Science*, *51*(12), 785–795. doi:
951 10.1016/j.pss.2003.05.002
- 952 Mazelle, C., Meziane, K., Mitchell, D. L., Garnier, P., Espley, J. R., Hamza,
953 A. M., ... Jakosky, B. M. (2018). Evidence for neutrals-foreshock elec-
954 trons impact at mars. *Geophysical Research Letters*, *45*(9), 3768–3774. doi:
955 10.1002/2018GL077298
- 956 Mazelle, C., & Neubauer, F. M. (1993). Discrete wave packets at the proton cy-
957 clotron frequency at comet p/halley. *Geophysical Research Letters*, *20*(2), 153–
958 156. doi: 10.1029/92GL02613
- 959 Mazelle, C., Winterhalter, D., Sauer, K., Trotignon, J. G., Acuna, M. H.,
960 Baumgärtel, K., ... Slavin, J. (2004). Bow shock and upstream phe-
961 nomena at mars. *Space Science Reviews*, *111*, 115–181. doi: 10.1023/B:
962 SPAC.0000032717.98679.d0
- 963 Meziane, K., Mazelle, C. X., Romanelli, N., Mitchell, D. L., Espley, J. R., Conner-
964 ney, J. E. P., ... Jakosky, B. M. (2017). Martian electron foreshock from
965 maven observations. *Journal of Geophysical Research: Space Physics*, *122*(2),
966 1531–1541. doi: 10.1002/2016JA023282
- 967 Modolo, R., Chanteur, G. M., Dubinin, E., & Matthews, A. P. (2005). Influence of
968 the solar euv flux on the martian plasma environment. *Annales Geophysicae*,
969 *23*(2), 433–444. doi: 10.5194/angeo-23-433-2005
- 970 Rahmati, A., Larson, D. E., Cravens, T. E., Lillis, R. J., Halekas, J. S., McFadden,
971 J. P., ... Jakosky, B. M. (2017). Maven measured oxygen and hydrogen pickup
972 ions: Probing the martian exosphere and neutral escape. *Journal of Geophys-
973 ical Research: Space Physics*, *122*(3), 3689–3706. doi: 10.1002/2016JA023371
- 974 Rahmati, A., Larson, D. E., Cravens, T. E., Lillis, R. J., Halekas, J. S., McFadden,
975 J. P., ... Jakosky, B. M. (2018). Seasonal variability of neutral escape from
976 mars as derived from maven pickup ion observations. *Journal of Geophysical
977 Research: Planets*, *123*(5), 1192–1202. doi: 10.1029/2018JE005560
- 978 Romanelli, N., Bertucci, C., Gomez, D., Mazelle, C., & Delva, M. (2013). Proton
979 cyclotron waves upstream from mars: observations from mars global surveyor.
980 *Planetary and Space Science*, *76*, 1–9. doi: 10.1016/j.pss.2012.10.011

- 981 Romanelli, N., Mazelle, C., Chaufray, J.-Y., Meziane, K., Shan, L., Ruhunusiri, S.,
 982 ... Jakosky, B. M. (2016). Proton cyclotron waves occurrence rate upstream
 983 from mars observed by maven: Associated variability of the martian upper
 984 atmosphere. *Journal of Geophysical Research: Space Physics*, *121*(11), 11,113–
 985 11,128. doi: 10.1002/2016JA023270
- 986 Romanelli, N., Mazelle, C., & Meziane, K. (2018). Nonlinear wave-particle inter-
 987 action: Implications for newborn planetary and backstreaming proton veloc-
 988 ity distribution functions. *Journal of Geophysical Research: Space Physics*,
 989 *123*(2), 1100–1117. doi: 10.1002/2017JA024691
- 990 Ruhunusiri, S., Halekas, J. S., Connerney, J. E. P., Espley, J. R., McFadden, J. P.,
 991 Larson, D. E., ... Jakosky, B. M. (2015). Low-frequency waves in the
 992 martian magnetosphere and their response to upstream solar wind driv-
 993 ing conditions. *Geophysical Research Letters*, *42*(21), 8917–8924. doi:
 994 10.1002/2015GL064968
- 995 Ruhunusiri, S., Halekas, J. S., Connerney, J. E. P., Espley, J. R., McFadden, J. P.,
 996 Mazelle, C., ... others (2016). Maven observation of an obliquely propagating
 997 low-frequency wave upstream of mars. *Journal of Geophysical Research: Space*
 998 *Physics*, *121*(3), 2374–2389. doi: 10.1002/2015JA022306
- 1000 Russell, C. T., Luhmann, J. G., Schwingenschuh, K., Riedler, W., & Yeroshenko, Y.
 1001 (1990). Upstream waves at mars: Phobos observations. *Geophysical Research*
 1002 *Letters*, *17*(6), 897–900. doi: 10.1029/GL017i006p00897
- 1003 Sánchez-Lavega, A., del Río-Gaztelurrutia, T., Hernández-Bernal, J., & Delcroix, M.
 1004 (2019). The onset and growth of the 2018 martian global dust storm. *Geophys-*
 1005 *ical Research Letters*, *46*(11), 6101–6108. doi: 10.1029/2019GL083207
- 1006 Smith, M. D. (2009). Themis observations of mars aerosol optical depth from 2002–
 1007 2008. *Icarus*, *202*(2), 444–452. doi: 10.1016/j.icarus.2009.03.027
- 1008 Smith, M. D., & Guzewich, S. D. (2019). The mars global dust storm of 2018. In
 1009 *49th international conference on environmental systems*. Boston, MA (USA).
- 1010 Song, P., & Russell, C. T. (1999). Time series data analyses in space physics. *Space*
 1011 *Science Reviews*, *87*(3–4), 387–463. doi: 10.1023/A:1005035800454
- 1012 Sonnerup, B. U. O., & Scheible, M. (1998). Minimum and maximum variance analy-
 1013 sis. *Analysis methods for multi-spacecraft data*, *1*, 185–220.
- Thiemann, E. M. B., Chamberlin, P. C., Eparvier, F. G., Templeman, B., Woods,

- 1014 T. N., Bougher, S. W., & Jakosky, B. M. (2017). The maven evm model
1015 of solar spectral irradiance variability at mars: Algorithms and results.
1016 *Journal of Geophysical Research: Space Physics*, 122(3), 2748–2767. doi:
1017 10.1002/2016JA023512
- 1018 Tsurutani, B. T. (1991). Comets: A laboratory for plasma waves and insta-
1019 bilities. In A. Johnstone (Ed.), *Cometary plasma processes* (Vol. 61, pp.
1020 189–209). Washington, D.C.: American Geophysical Union (AGU). doi:
1021 10.1029/GM061p0189
- 1022 Wei, H. Y., Cowee, M. M., Russell, C. T., & Leinweber, H. K. (2014). Ion cyclotron
1023 waves at mars: Occurrence and wave properties. *Journal of Geophysical Re-*
1024 *search: Space Physics*, 119(7), 5244–5258. doi: 10.1002/2014JA020067
- 1025 Wei, H. Y., & Russell, C. T. (2006). Proton cyclotron waves at mars: Exosphere
1026 structure and evidence for a fast neutral disk. *Geophysical Research Letters*,
1027 33(23), L23103. doi: 10.1029/2006GL026244
- 1028 Wei, H. Y., Russell, C. T., Zhang, T. L., & Blanco-Cano, X. (2011). Comparative
1029 study of ion cyclotron waves at mars, venus and earth. *Planetary and Space*
1030 *Science*, 59(10), 1039–1047. doi: 10.1016/j.pss.2010.01.004
- 1031 Wu, C. S., & Davidson, R. C. (1972). Electromagnetic instabilities produced by
1032 neutral-particle ionization in interplanetary space. *Journal of Geophysical Re-*
1033 *search*, 77(28), 5399–5406. doi: 10.1029/JA077i028p05399
- 1034 Wu, C. S., & Hartle, R. E. (1974). Further remarks on plasma instabilities produced
1035 by ions born in the solar wind. *Journal of Geophysical Research*, 79(1), 283–
1036 285. doi: 10.1029/JA079i001p00283
- 1037 Yamauchi, M., Hara, T., Lundin, R., Dubinin, E., Fedorov, A., Sauvaud, J.-A.,
1038 ... others (2015). Seasonal variation of martian pick-up ions: Evidence
1039 of breathing exosphere. *Planetary and Space Science*, 119, 54–61. doi:
1040 10.1016/j.pss.2015.09.013
- 1041 Zhang, M. H. G., Luhmann, J. G., Nagy, A. F., Spreiter, J. R., & Stahara, S. S.
1042 (1993). Oxygen ionization rates at mars and venus: Relative contributions
1043 of impact ionization and charge exchange. *Journal of Geophysical Research:*
1044 *Planets*, 98(E2), 3311–3318. doi: 10.1029/92JE02229
- 1045 Zhang, T. L., Delva, M., Baumjohann, W., Volwerk, M., Russell, C. T., Barabash,
1046 S., ... Kudela, K. (2008). Initial venus express magnetic field observations of

1047

the venus bow shock location at solar minimum. *Planetary and Space Science*,

1048

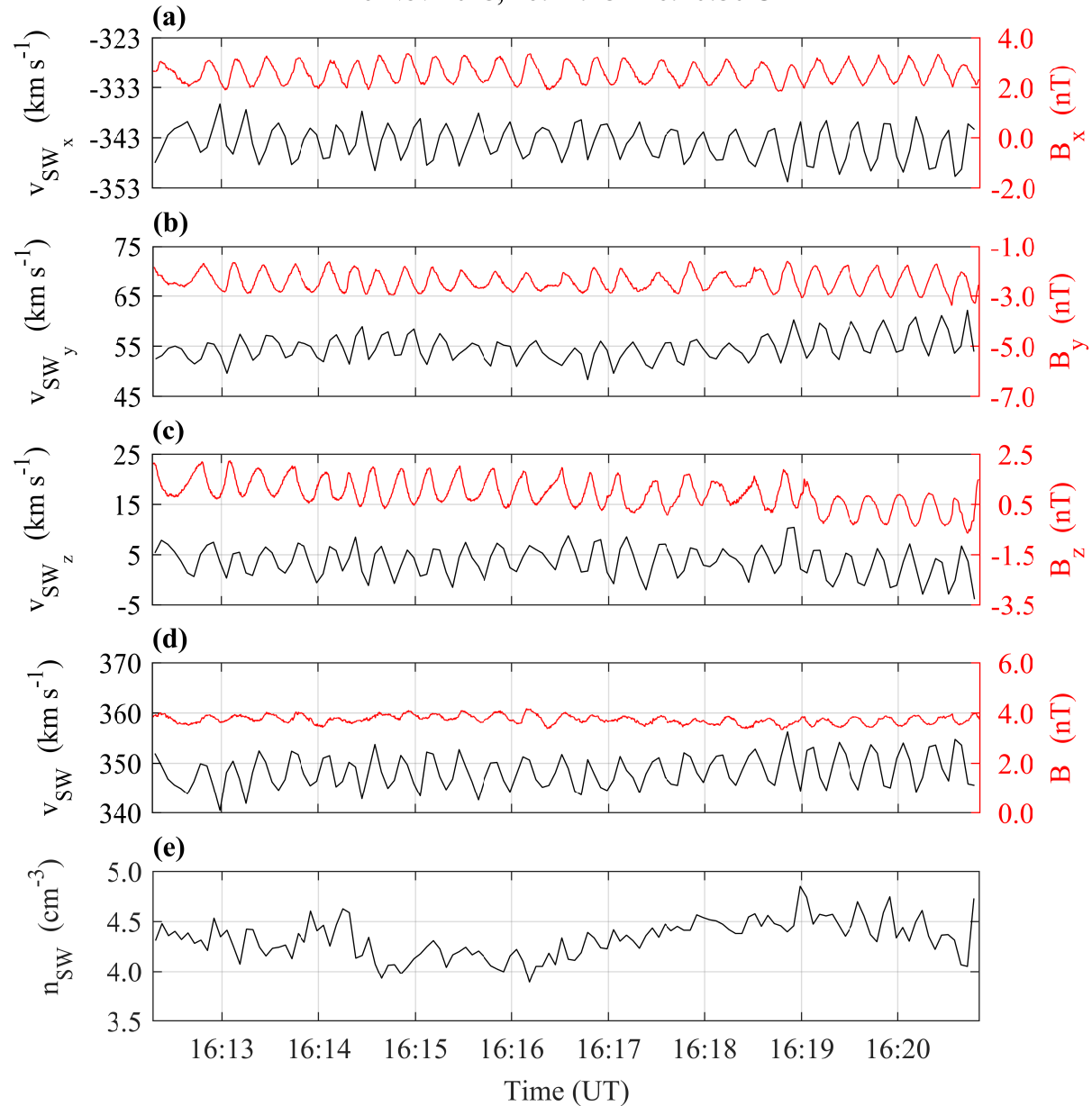
56(6), 785–789. doi: 10.1016/j.pss.2007.09.012

Accepted Article

Figure1.

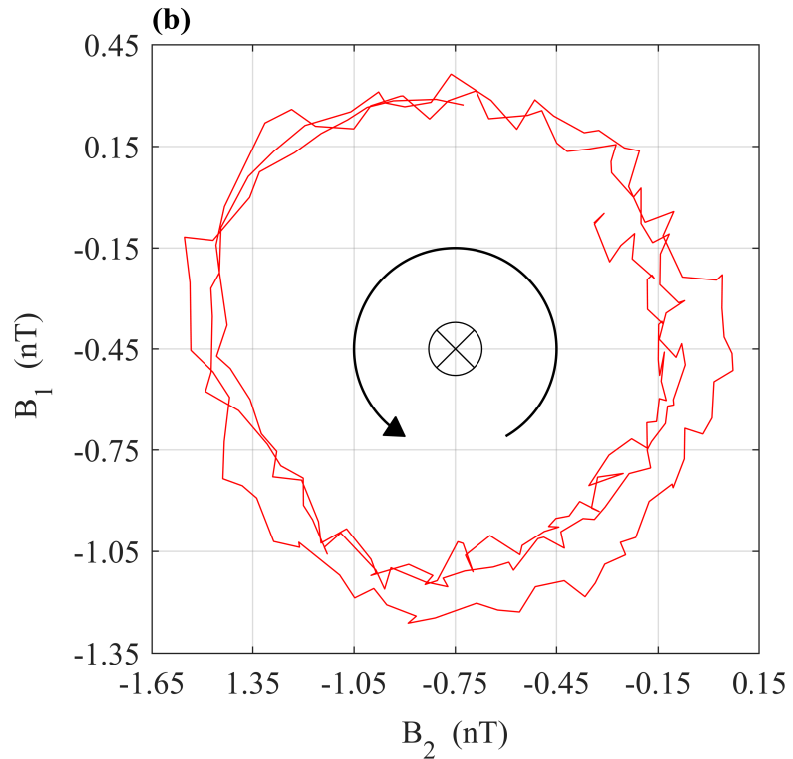
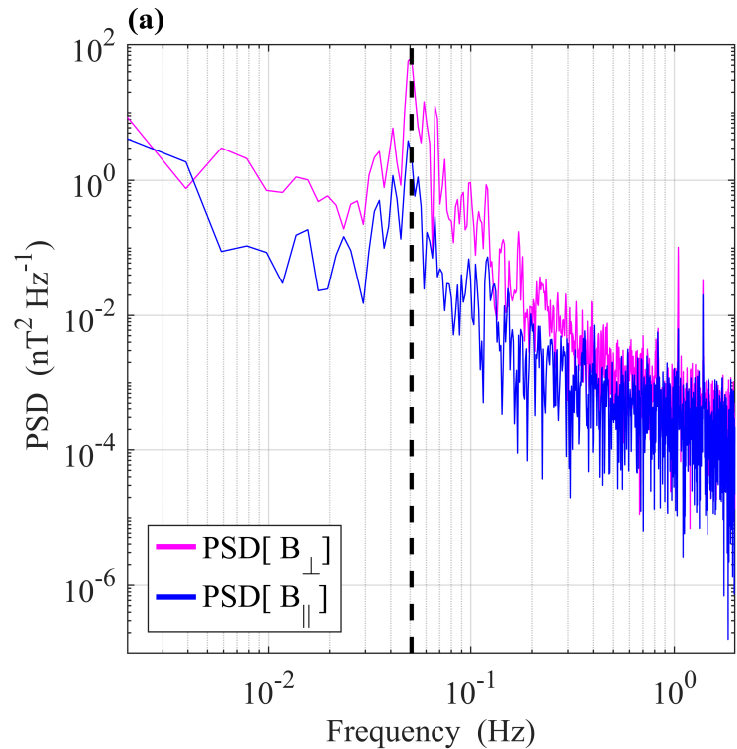
Accepted Article

**MAVEN MAG and SWIA Observations (MSO Coordinates):
26 Nov 2018, 16:12:18 - 16:20:50 UT**



Accepted Article

PSD and MVA of MAVEN MAG Observations: 26 Nov 2018, 16:12:18 - 16:20:50 UT



Accepted Article

PCW Occurrence Rate Upstream from the Martian Bow Shock (Oct 2014 - Feb 2020)

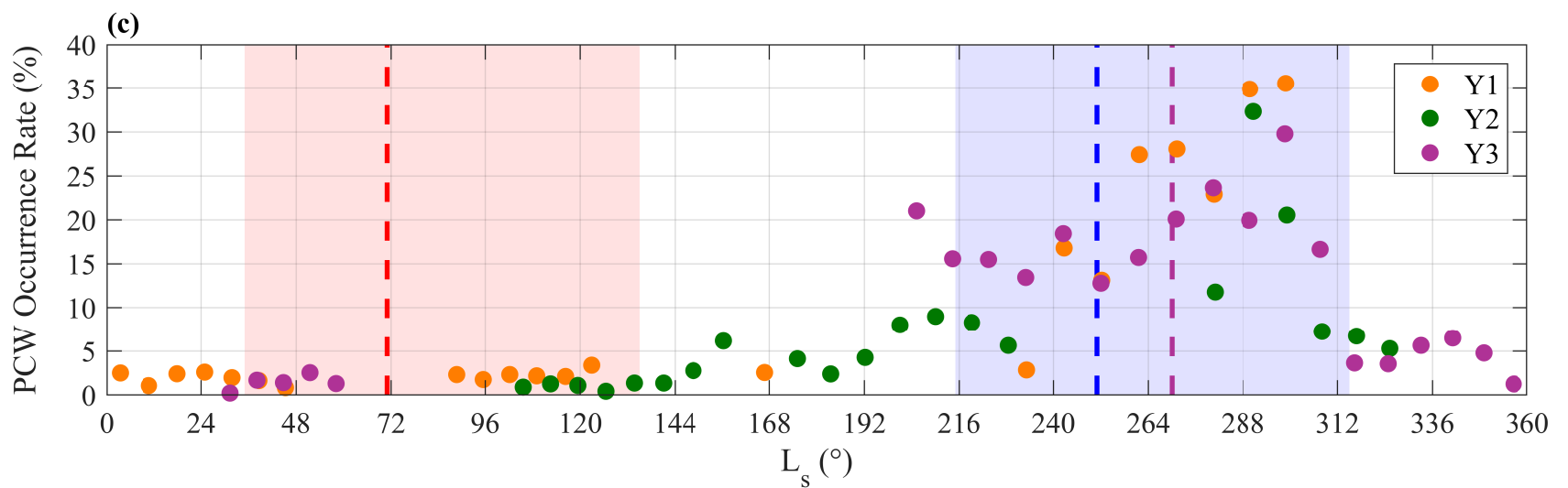
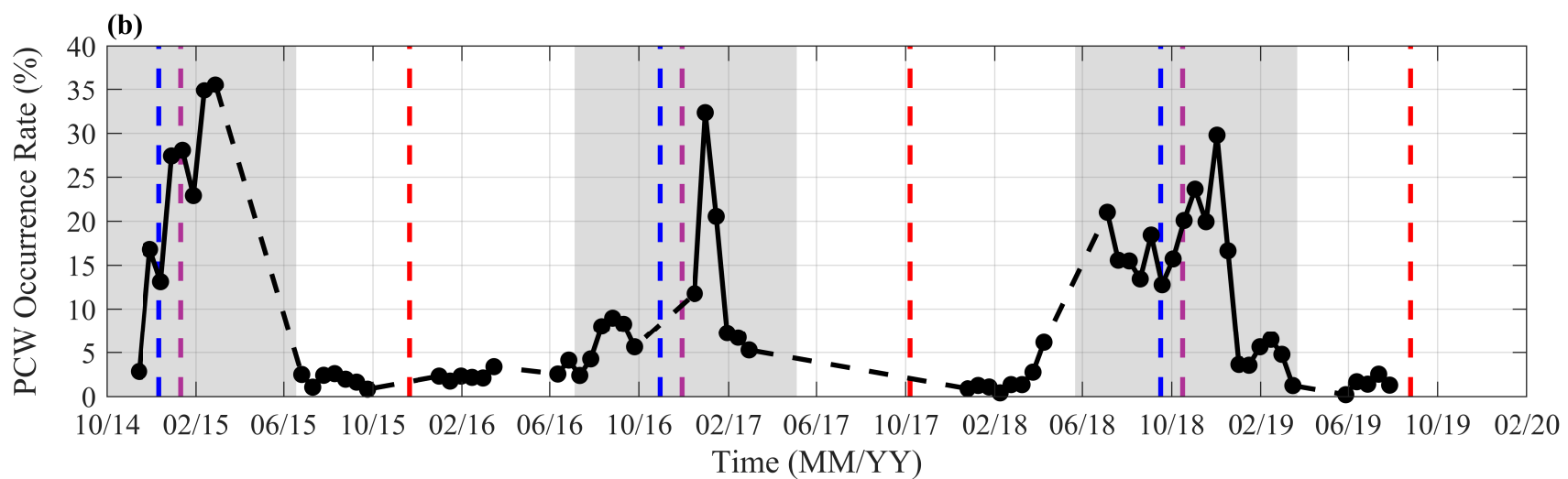
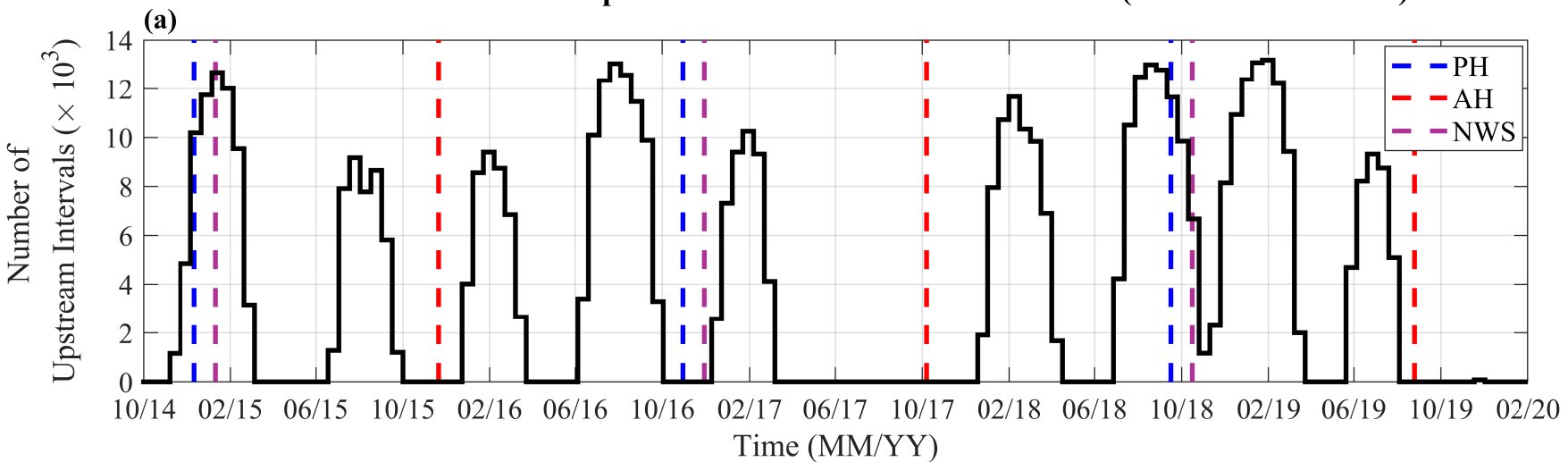
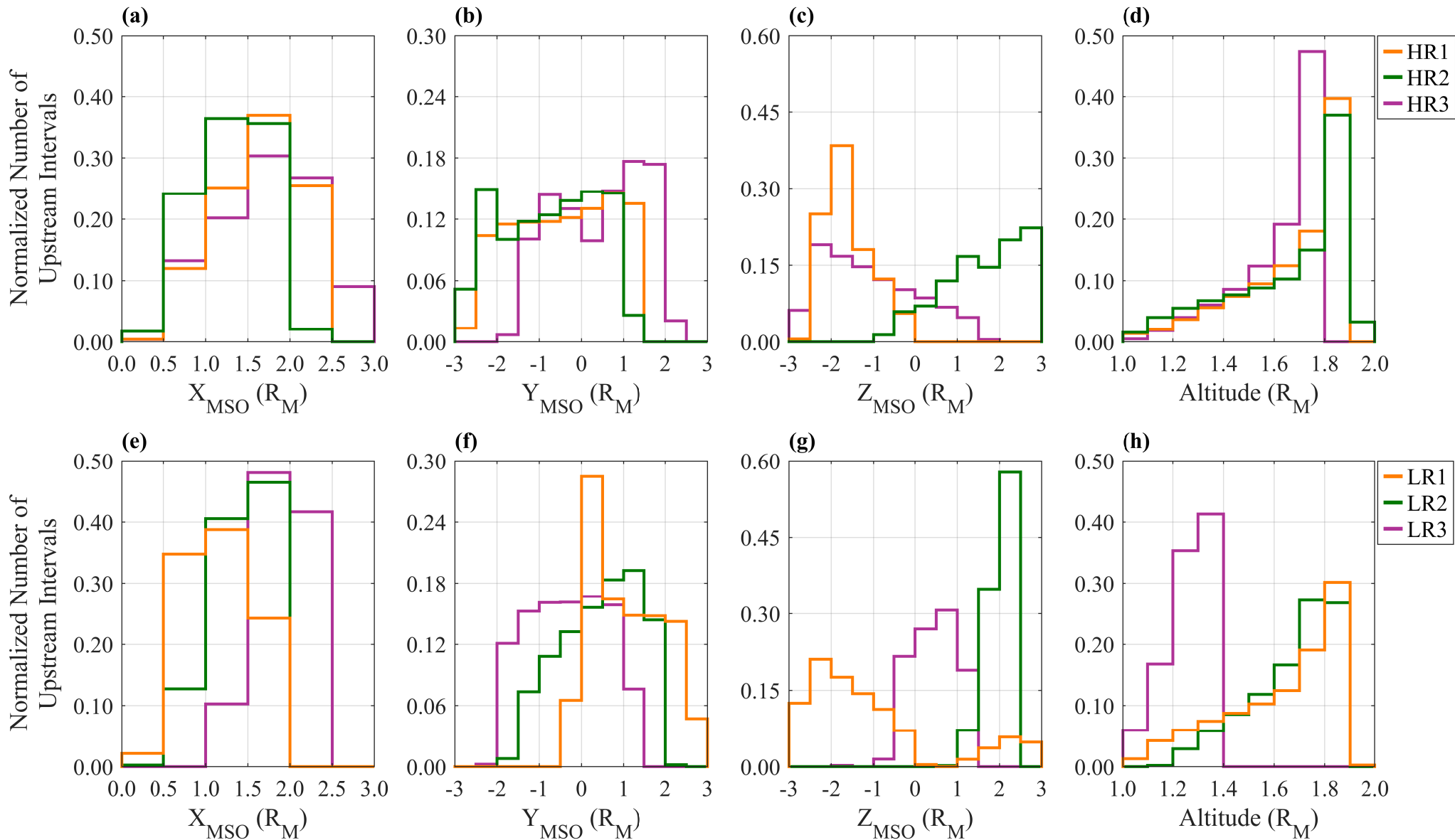


Figure4.

Accepted Article

MAVEN Spatial Distribution Upstream from the Martian Bow Shock (HR and LR Groups)



Accepted Article

PCW Probability Distribution $P(x)$ Upstream from the Martian Bow Shock (Oct 2014 - Feb 2020)

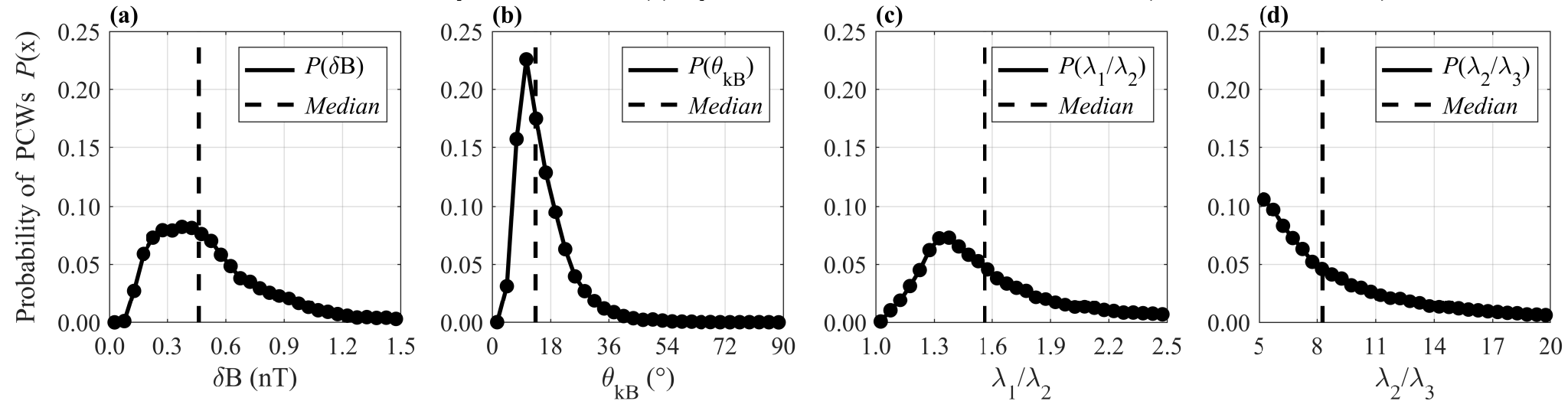
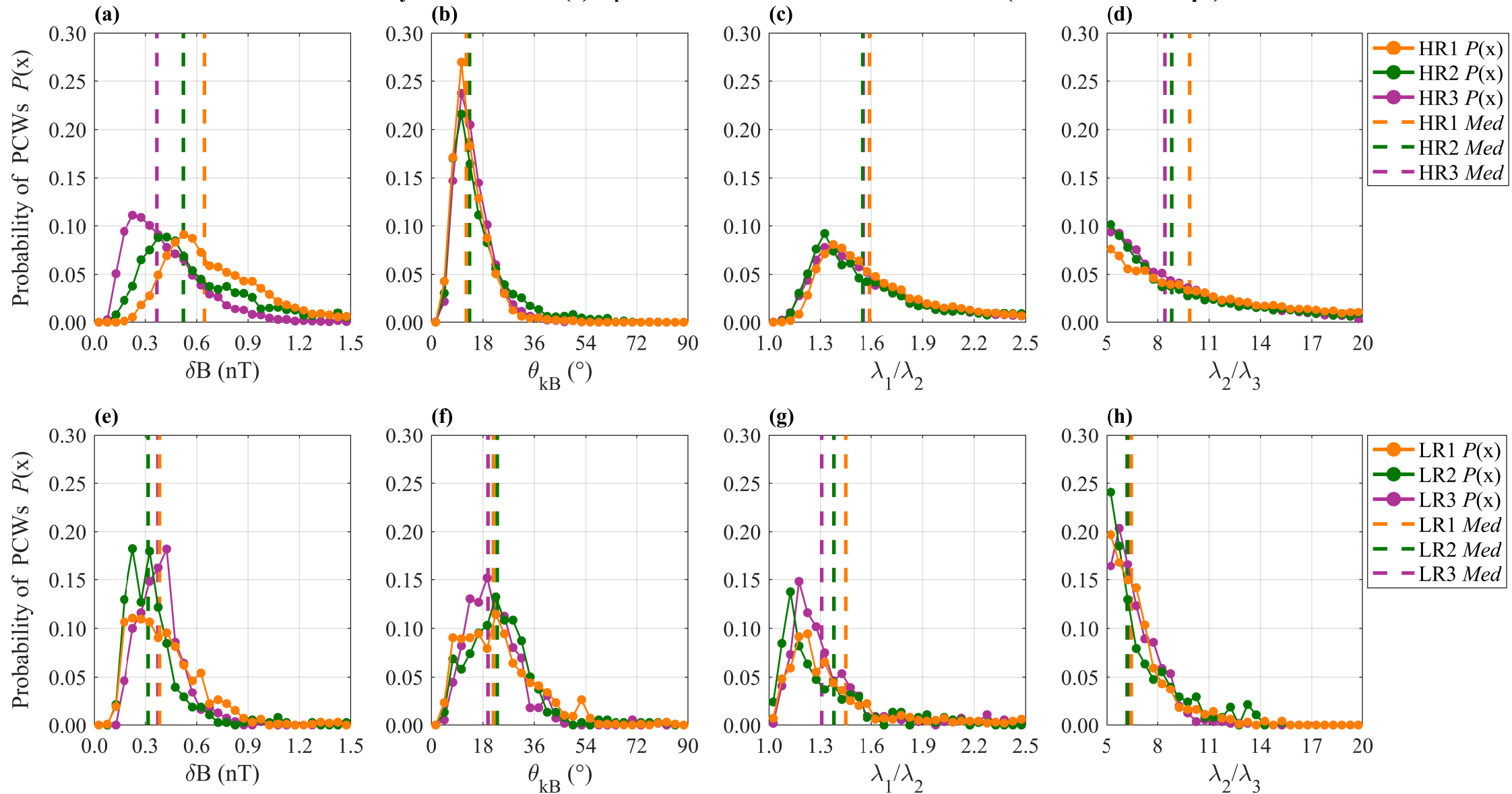


Figure6.

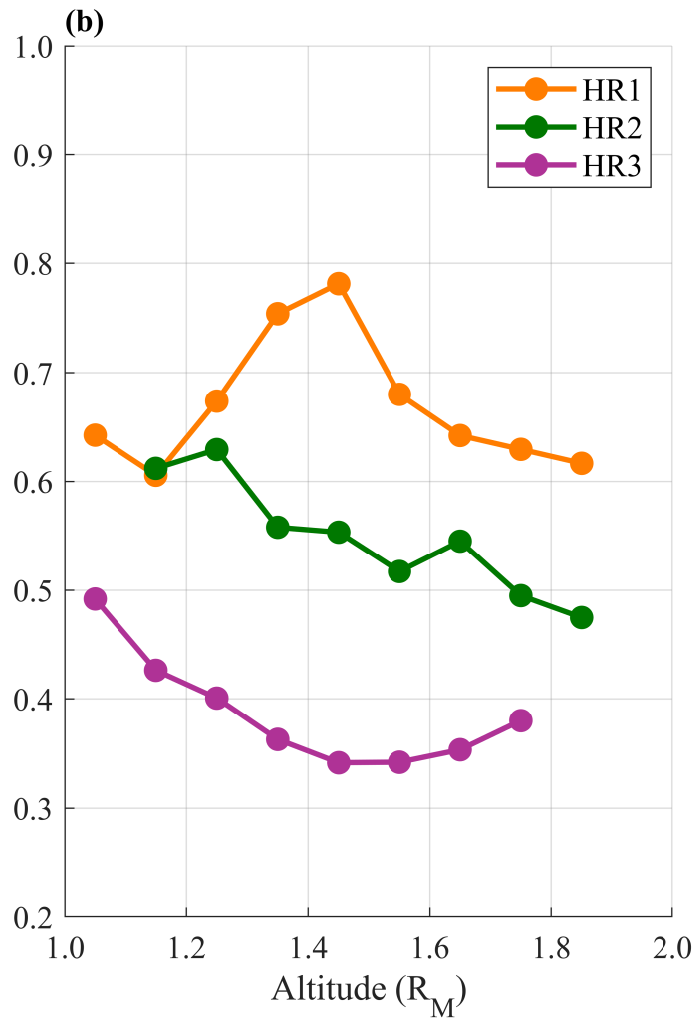
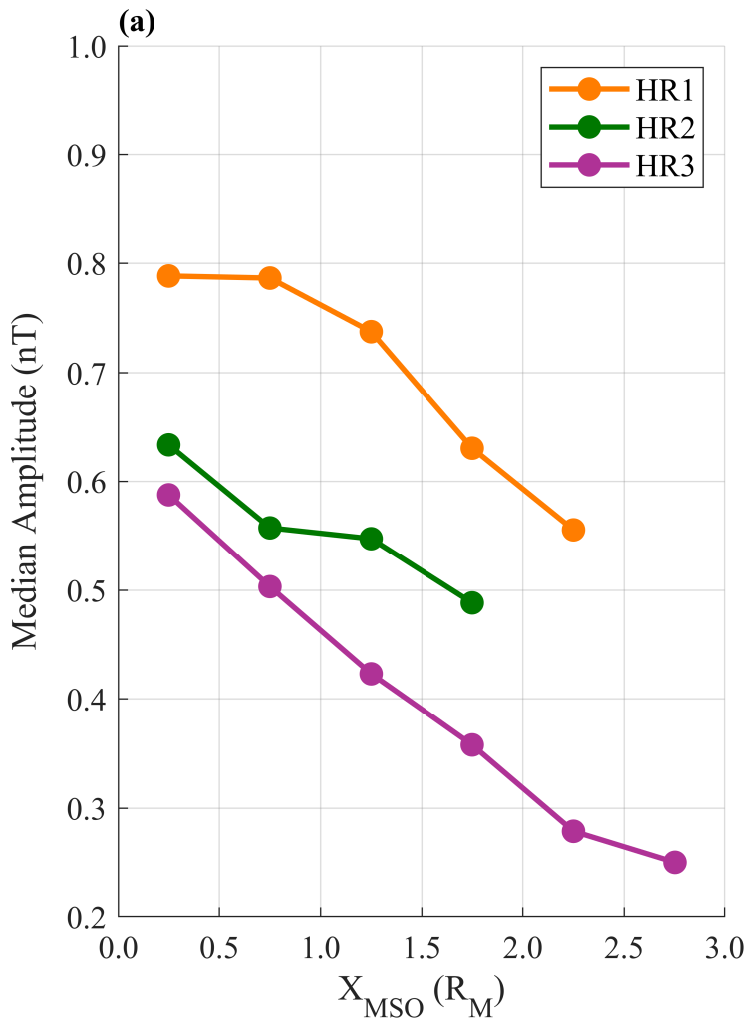
Accepted Article

PCW Probability Distribution $P(x)$ Upstream from the Martian Bow Shock (HR and LR Groups)



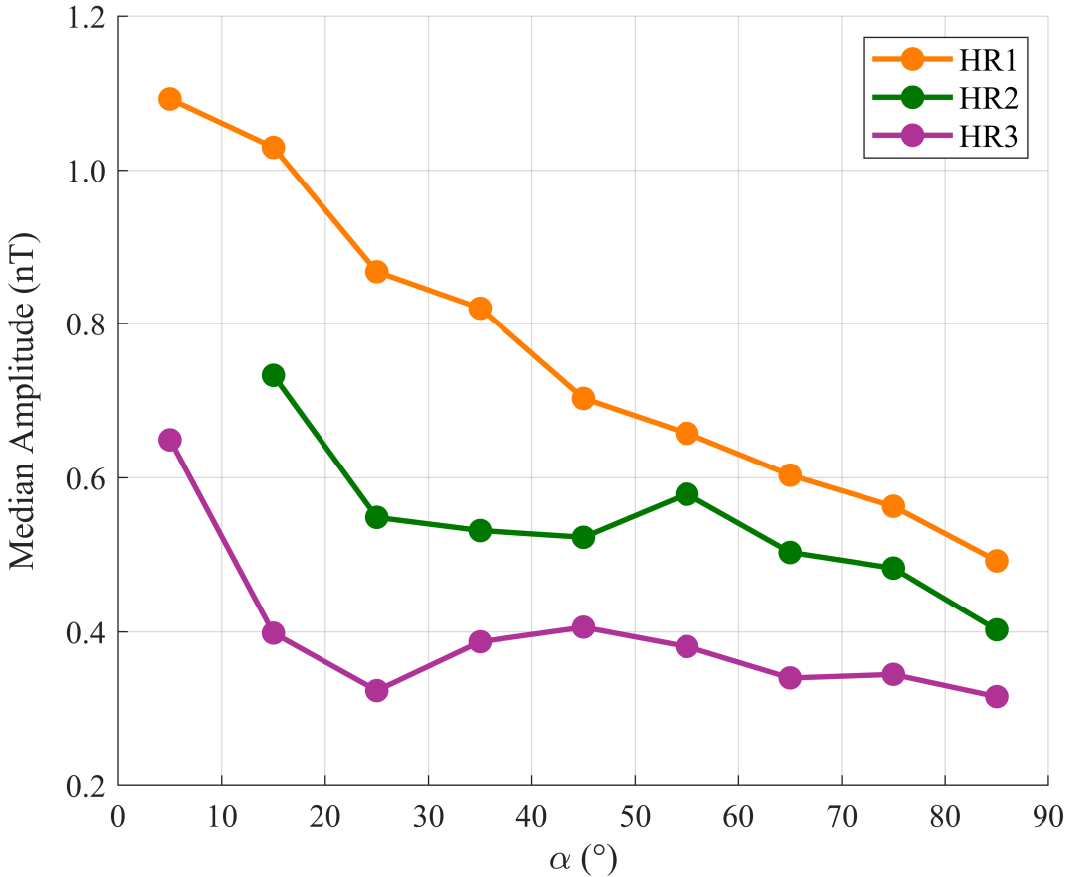
Accepted Article

Spatial Distribution of PCW Amplitude Upstream from the Martian Bow Shock (HR Groups)



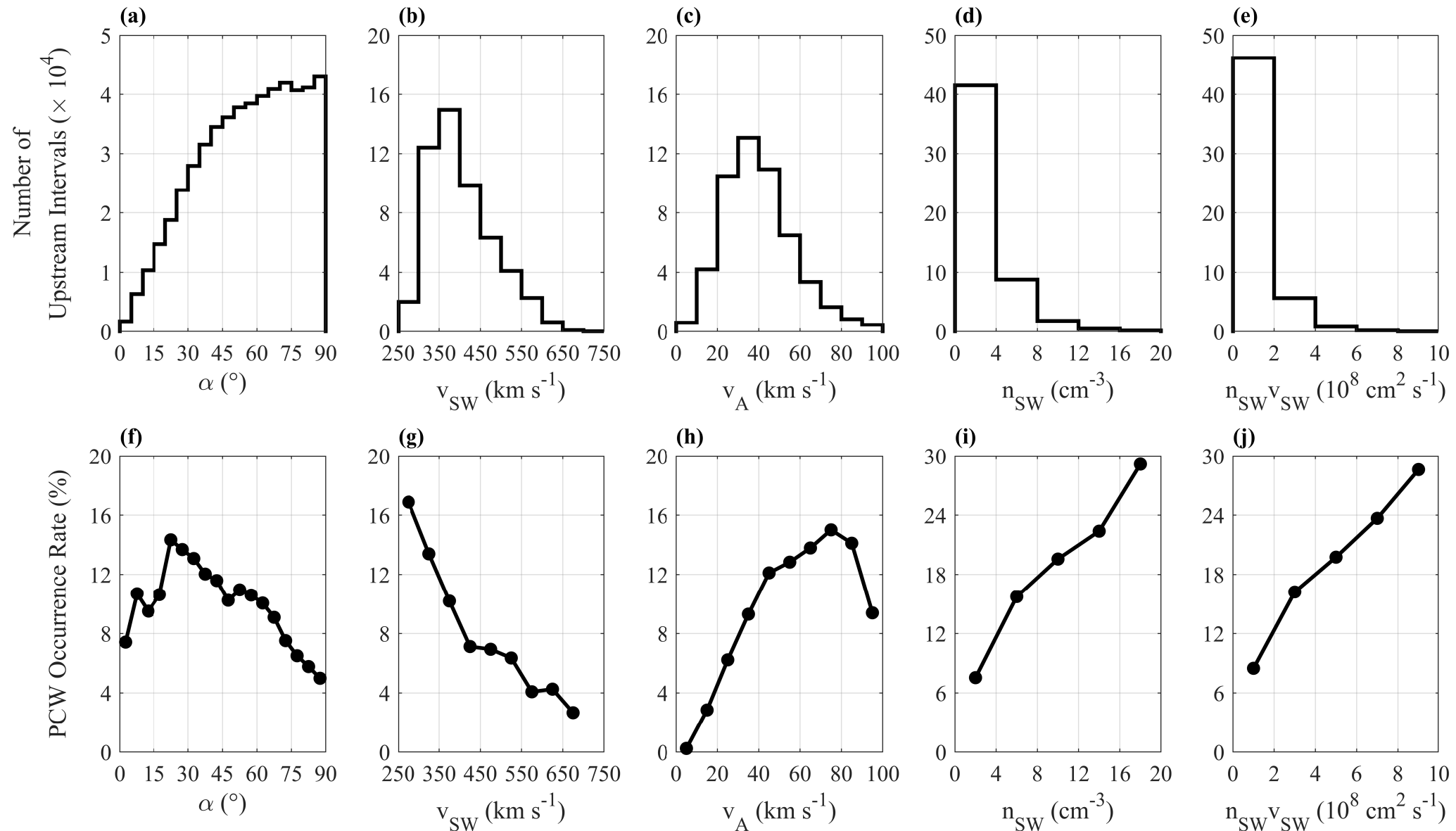
Accepted Article

PCW Amplitude Upstream from the Martian Bow Shock (HR Groups)



Accepted Article

PCW Occurrence Rate for Solar Wind Conditions Upstream from the Martian Bow Shock (Oct 2014 - Feb 2020)



Accepted Article

PCW Occurrence Rate for Solar Wind Conditions Upstream from the Martian Bow Shock (HR Groups)

